

Lower limit for differential rotation in members of young loose stellar associations

E. Distefano¹, A. C. Lanzafame², A. F. Lanza¹, S. Messina¹, and F. Spada³

¹ INAF - Osservatorio Astrofisico di Catania

Via S. Sofia, 78, 95123, Catania, Italy

e-mail: elisa.distefano@oact.inaf.it

² University of Catania, Astrophysics Section, Dept. of Physics and Astronomy

Via S. Sofia, 78, 95123, Catania, Italy

³ Leibniz-Institut für Astrophysik Potsdam (AIP)

An der Sternwarte 16, D-14482, Potsdam, Germany

Received ; accepted

ABSTRACT

Context. Surface differential rotation (SDR) plays a key role in dynamo models and determines a lower limit on the accuracy of stellar rotation period measurements. SDR estimates are therefore essential for constraining theoretical models and inferring realistic rotation period uncertainties.

Aims. We measure a lower limit to SDR in a sample of solar-like stars belonging to young loose stellar associations with the aim of investigating how SDR depends on global stellar parameters in the age range (4 – 95 Myr).

Methods. The rotation period of a solar-like star can be recovered by analyzing the flux modulation caused by dark spots and stellar rotation. The SDR and the latitude migration of dark-spots induce a modulation of the detected rotation period. We employ long-term photometry to measure the amplitude of such a modulation and to compute the quantity $\Delta\Omega_{\text{phot}} = \frac{2\pi}{P_{\text{min}}} - \frac{2\pi}{P_{\text{max}}}$ that is a lower limit to SDR.

Results. We find that $\Delta\Omega_{\text{phot}}$ increases with the stellar effective temperature and with the global convective turn-over time-scale τ_c , that is the characteristic time for the rise of a convective element through the stellar convection zone. We find that $\Delta\Omega_{\text{phot}}$ is proportional to $T_{\text{eff}}^{2.18 \pm 0.65}$ in stars recently settled on the ZAMS. This power law is less steep than those found by previous authors, but closest to recent theoretical models. We investigate how $\Delta\Omega_{\text{phot}}$ changes in time in $\sim 1 M_{\odot}$ star. We find that $\Delta\Omega_{\text{phot}}$ steeply increases between 4 and 30 Myr and that it is almost constant between 30 and 95 Myr. We find also that the relative shear increases with the Rossby number Ro . Although our results are qualitatively in agreement with hydrodynamical mean-field models, our measurements are systematically higher than the values predicted by these models. The discrepancy between $\Delta\Omega_{\text{phot}}$ measurements and theoretical models is particularly large in stars with periods between 0.7 and 2 d. Such a discrepancy, together with the anomalous SDR measured by other authors for HD 171488 (rotating in 1.31 d), suggests that the rotation period could influence SDR more than predicted by the models.

Key words. stars: solar-type – stars :starspots– stars: rotation– galaxy: open clusters and associations: general– techniques: photometric

1. Introduction

Surface differential rotation (here after SDR) has been detected and measured in a wide sample of solar-like stars (e.g. Barnes et al. 2005; Collier Cameron 2007; Reinhold et al. 2013). These measurements are essential to constrain theoretical models that try to investigate the connections between rotation, convection and topology of stellar magnetic fields. The amplitude of SDR influences the kind of dynamo operating inside the star. Indeed, differential rotation is able to generate a strong toroidal magnetic field out a weak poloidal field and, therefore, is a key ingredient of $\alpha\Omega$ dynamos (e.g. Parker 1955; Brandenburg et al. 1991). On the other hand, stars characterized by a low SDR degree and rotating as solid bodies can instead sustain only an α^2 -type dynamo (e.g. Moss & Brandenburg 1995; Küker & Rüdiger 2011).

The amplitude of SDR is usually measured through the surface rotational shear:

$$\Delta\Omega = \Omega_0 - \Omega_{\text{pole}} \quad (1)$$

where Ω_0 and Ω_{pole} are the surface angular velocities at equator and at poles, respectively. If $\Delta\Omega > 0$ then the star has a solar-like SDR, i.e. the equator rotates faster than poles. If $\Delta\Omega < 0$ the star exhibits an anti-solar SDR.

In recent years, several authors investigated how SDR depends on stellar effective temperature and rotation period. Barnes et al. (2005) report $\Delta\Omega$ measurements obtained by means of the Doppler imaging technique for a sample of ten young late-type stars. They find that $\Delta\Omega$ is strongly dependent on the stellar temperature ($\Delta\Omega \propto T_{\text{eff}}^{8.93 \pm 0.31}$) but poorly correlated to Ω_0 ($\Delta\Omega \propto \Omega_0^{0.15 \pm 0.1}$). A strong correlation between $\Delta\Omega$ and T_{eff} is also found by Collier Cameron (2007) who enlarges the sample of stars studied by Barnes et al. (2005) and finds the relationship $\Delta\Omega \propto T_{\text{eff}}^{8.6}$.

The results found by these works are in quantitative disagreement with theoretical models developed by Kitchatinov & Rüdiger (1999), Küker & Rüdiger (2011) and by Küker et al. (2011). Such theoretical works predict that SDR increases with the stellar temperature and that it is almost independent on the stellar rotation period. However, the power law expected from these models is $\Delta\Omega \propto (\frac{T_{\text{eff}}}{5500\text{K}})^2$ in the range 3800 – 6000 K and $\Delta\Omega \propto (\frac{T_{\text{eff}}}{5500\text{K}})^{20}$ above 6000 K (Küker & Rüdiger 2011).

Reinhold et al. (2013) analyze the Quarter 3 (Q3) long cadence photometric data collected by the Kepler mission (Borucki et al. 2010) and search for SDR in a sample of about 20000 main-sequence late-type stars. In contrast with Barnes et al. (2005) and Collier Cameron (2007), they find that SDR exhibits a weak dependence on temperature in the range 3800 – 6000 K and that, above 6000 K, it steeply increases towards higher temperatures. Reinhold et al. (2013) claim that their results, though quite scattered, are in better agreement with the model of Küker & Rüdiger (2011). Note however that these authors have no information on the ages of their targets. This lack of information makes it difficult to compare their results with those of Barnes et al. (2005) and Collier Cameron (2007). Indeed, the targets investigated by Barnes et al. (2005) and Collier Cameron (2007) comprise pre-main-sequence stars and stars recently settled in ZAMS while the sample of Reinhold et al. (2013) includes field stars of different ages. Moreover their data do not permit to study SDR as a function of the stellar age.

The present work is focused on a sample of 111 late-type stars belonging to 11 nearby young loose associations with known ages (Table 1). The ages of these associations span the interval (4 – 95 Myr) and therefore our study concerns the SDR evolution during the transition between the Pre-Main-Sequence and the Main-Sequence phase. We search for SDR by analyzing long-term photometric time-series collected by ASAS (All Sky Automatic Survey, Pojmanski 1997) and SuperWASP (Wide Angle Search for Planets, Pollacco et al. 2006).

The paper is organized in the following way: in Sect. 2 we describe the photometric data; in Sect. 3 we explain the method we employed to measure the quantity $\Delta\Omega_{\text{phot}}^1$, that is a lower limit for SDR; in Sect. 4 we investigate how $\Delta\Omega_{\text{phot}}$ depends on global stellar parameters; in Sect. 5 we discuss the main results of our study and in Sec. 6 the conclusions are drawn.

2. Data

Messina et al. (2010, 2011) analyze ASAS and SuperWASP time-series for about 300 stars belonging to nearby young associations and measure the rotation period for most of these stars. In this work we reprocess 99 ASAS time-series and 31 SuperWASP time-series with a new technique (see Sect. 3) for estimating a lower limit $\Delta\Omega_{\text{phot}}$ for the rotational shear. In Table 2 we list the 111 stars studied here together with their colour indexes and spectral types. These targets have been selected among those studied in Messina et al. (2010, 2011) by picking up those for which the largest number of photometric measurements is available. For nine of these targets both ASAS and SuperWASP time-series are available. Note that the ASAS time-series processed here span an interval time longer than those processed in Messina et al. (2010, 2011).

¹ The subscript stands for photometric and indicates the kind of data used to measure SDR.

2.1. ASAS photometry

The ASAS time-series analyzed in the present work are contained in the ASAS-3 Photometric V-band catalogue². These time-series cover a time-span of about 13 years (from 1997 to 2010) and have a typical photometric error of 0.02 mag. This error allows the detection of rotational modulation in young solar-like stars where the amplitude modulation ranges between 0.05 and 0.3 mags (Messina et al. 2011). In our analysis we use filtered time-series obtained by selecting only the best photometric data. The time-series sampling depends on the star coordinates. We divide the ASAS time-series into three groups for which the average interval t_{mean} between two consecutive observations is $\approx 1, 2$ and 3 days, respectively.

2.2. SuperWASP photometry

The SuperWASP time-series have been downloaded from the first public data archive (Butters et al. 2010). These time-series cover a time span of about four years (from 2004 to 2008). Their time coverage is quite irregular and depends on the sky coordinates. The time-series processed in the present work are typically made of two or three distinct observational seasons covering 60-300 d intervals. During each season a target is observed every day for a few hours with a sampling rate of about ten minutes in the most favorable sky positions. The SuperWASP data have therefore a better sensitivity to periods ≤ 1 d than the ASAS data. Our analysis is based on the processed flux measurements obtained through application of the SYSREM algorithm (Tamuz et al. 2005). SuperWASP observations were collected in 2004 without any light filter. Starting from 2006, they were collected through a wide band filter in the range 400 – 700 nm. Owing to differences in spectral bands with respect to the standard Johnson V ASAS data, we analyze the SuperWASP data independently without merging them with ASAS data.

3. The method

The surface of a solar-like star is covered by magnetically Active Regions (hereafter ARs) associated with dark spots and bright faculae. If the star is a differential rotator, the ARs will rotate with different frequencies, depending on their latitudes, and will modulate the optical flux coming from the star. ARs migration in latitude induces a modulation of the measured photometric period that can be used for estimating the amplitude of SDR. Based on this, the method we employ to measure SDR on a given star consists in the followings steps:

- we segment the photometric time-series with a "sliding-window" algorithm;
- we search for the stellar rotation period in each segment;
- we pick up the maximum and the minimum detected periods and we compute the quantity $\Delta\Omega_{\text{phot}} = \Omega_{\text{max}} - \Omega_{\text{min}}$ where $\Omega_{\text{max}} = \frac{2\pi}{P_{\text{min}}}$ and $\Omega_{\text{min}} = \frac{2\pi}{P_{\text{max}}}$.

We assume P_{max} and P_{min} are related to time-series segments where the stellar surface is dominated by high latitude and low latitude ARs, respectively (or by the opposite configuration in the case of an anti-solar SDR). Since the P_{max} and P_{min} thus found do not necessarily sample the whole latitude range, $\Delta\Omega_{\text{phot}}$ is obviously a lower limit for the rotational shear and therefore $\Delta\Omega_{\text{phot}} \leq \Delta\Omega$.

² <http://www.astrouw.edu.pl/asas/>

Table 1. Stellar associations investigated in the present work.

Association	N.	age (Myr)	Ref.
ϵ Chamaleontis (ϵ Cha)	9	3-5	1, 2
η Chamaleontis (η Cha)	4	6-10	1, 3, 4
TW Hydrae (TWA)	9	8-12	5, 6
β Pictoris (β Pic)	18	12-22	7, 8
Octans (Oct)	1	20-40	9, 10
Columba (Col)	14	20-40	11, 12
η Carinae (η Car)	12	20-40	11, 12
Tucana-Horologium (Tuc/Hor)	17	20-40	11, 12
Argus (Arg)	10	30-50	9, 13, 14
IC 2391	3	30-50	13, 14
AB Doradus (AB Dor)	14	70-120	15, 16, 17

Notes. For each association we report the number of members for which we estimated $\Delta\Omega_{\text{phot}}$, the ages estimate and the age reference. References: (1) Murphy et al. (2013); (2) Feigelson et al. (2003); (3) Mamajek et al. (1999); (4) Lawson & Feigelson (2001); (5) Webb et al. (1999); (6) Barrado Y Navascués (2006); (7) Song et al. (2003); (8) Makarov (2007); (9) Torres et al. (2008); (10) Murphy & Lawson (2015); (11) Torres et al. (2001); (12) Zuckerman & Webb (2000); (13) De Silva et al. (2013); (14) Barrado y Navascués et al. (2004); (15) Mentuch et al. (2008); (16) López-Santiago et al. (2006); (17) Luhman et al. (2005).

3.1. Time-series segmentation

Time-series segmentation is very useful in dealing with magnetically active stars. In fact, the typical light curves of these variables are not very regular because the flux variation due to rotational modulation can be masked by the intrinsic evolution of ARs.

In the Sun, ARs evolve on a typical time-scale $\tau_{\text{AR}} \approx 60$ d (Lanza et al. 2003). This time-scale, that is about twice the Sun rotation period, and the simultaneous occurrence of different ARs over the solar-disk could, in principle, destroy the coherence of the rotational signal and prevent the detection of the rotation period. However ARs tend to form, in the Sun, at active longitudes i.e. heliographic longitudes characterized by the frequent, localized emergence of new magnetic flux. These AR complexes (ARCs), forming at active longitudes, evolve in a typical time-scale $\tau_{\text{ARC}} \approx 200 - 250$ d (Lanza et al. 2003). Hence, the rotational signal is approximatively coherent on time intervals of the same order as τ_{ARC} . Lanza et al. (2004) analyze the TSI (Total Solar Irradiance) time-series collected by the SoHo satellite and show that the use of period-search algorithms to detect the rotation period of the Sun is only possible if the long term time-series is divided into sub-series with a time extension no longer than 150 d in order to limit the effect of the evolution of ARCs.

The time-scales of ARs and ARCs evolution in late-type stars other than the Sun have been studied to a limited extent because of the lack of multi-years continuous photometric time-series. Donahue et al. (1997a,b) estimated the time-scales of ARs evolution in some tens of late-type stars by analyzing long-term time-series of photometric fluxes in two 0.1 nm passbands centered on the Ca II H and K emission lines. They show that the older and less magnetically active stars tend to be "AR evolution-dominated". This means that the evolution of ARs and ARCs take place on time-scales comparable with the stellar rotation period. The light curves of younger and more active stars, conversely, exhibit a pattern that remains stable for several consecutive rotations. The typical time-scales measured for these stars are $\tau_{\text{AR}} = 50$ d and $\tau_{\text{ARC}} = 1$ yr. Similar values are reported by Hussain (2002). Messina & Guinan (2003) analyze long-term photometric time-series collected in the *Johnson* V band for six young solar analogues. They find that 2 of these

stars are evolution-dominated, while the others have τ_{ARC} values ranging between 160 d and 500 d, remarkably longer than their rotation periods.

The advantage of using time-series segments is that the data exhibit a more stable pattern of flux variations than the whole time-series, however, they also contain less points. Therefore, the rotation period retrieved by analyzing a time-series segment could have a low statistical significance. A compromise has been found between the length of the segments and the number of points included in the segments by adopting a length $T = 50$ d. In the case of ASAS data, the average number of points per segment range between 16 and 50, depending on the source coordinate. In the case of Super-WASP data, the average number of points per segment range between 1000 and 3000. Note that $T = 50$ d is also the typical τ_{AR} time-scale found by Donahue et al. (1997a) for young active stars. In Sec. 3.5 we discuss how the choice of different segments duration can affect $\Delta\Omega_{\text{phot}}$ measurements.

We perform the time-series segmentation by using a sliding window algorithm as sketched in Fig. 1. This algorithm performs a cycle on the whole time-series. For each observation time t_i , a segment is generated by selecting all points in the time interval $[t_i, t_i + T]$, where T is the length of the window. A segment is rejected if it has less than 10 points or if it is a subset of another segment (this last case happens when the time-series exhibits gaps larger than the sliding window; see Fig. 1).

In Fig. 1 we show the V-Band time-series of the star ASAS J070030-7941.8. The observations span about nine years. The red and the green bullets mark the data processed by Messina et al. (2010). The different colors are used to display the segmentation performed in that work. The black crosses mark data collected after February 2008 and that were not processed by Messina et al. (2010). Messina et al. (2010) extracted 10 sub-series. Our sliding window algorithm allows the extraction of more segments.

3.2. Rotation period and SDR estimate

We perform period-search by means of the Lomb-Scargle periodogram, that has been found to be a highly efficient method in dealing with solar-like variables (Distefano et al. 2012). For each time-series segment we compute the periodogram and we select the period P with the highest power Z . We build the distri-

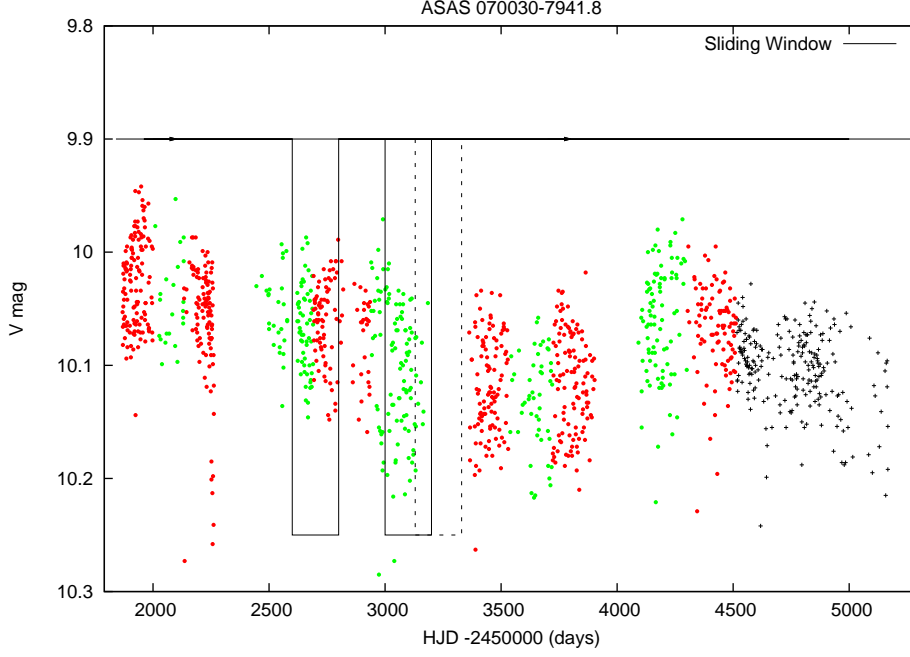


Fig. 1. A typical V-band time-series collected by the ASAS survey. The red and green bullets mark the segmentation performed by Messina et al. (2010). The black continuous boxes depict two of the extracted segments whereas the dotted box indicates one of the sub-series rejected by our segmentation algorithm. The black crosses mark data that have not been processed in Messina et al. (2010). Note that we employ a 50-day sliding window, whereas in the plot we sketch a 200-day sliding window in order to make the plot more clear.

bution of the detected periods and we estimate the average stellar rotation period by taking the mode of the distribution.

In the left panel of Fig. 2, we show the frequency histogram obtained for the source ASAS J070030-7941.8. The distribution exhibits a well defined peak at $P_{\text{rot}} = 5.12$ d that is taken as the average stellar rotation period. The other peaks occur at the beat periods B due to the interference between the rotational modulation and the typical ASAS 1-day sampling and are given by the relationship $B = P_{\text{rot}}/|1 \pm nP_{\text{rot}}|$ with $n = 1, 2, 3, \dots$

Once estimated the average rotation period, we perform again the period search by rejecting peaks close to the beat frequencies and selecting, for each segment, the highest significant peak closest to the average rotation period. We build the true period distribution and pick up P_{min} and P_{max} in order to compute $\Delta\Omega_{\text{phot}}$. In some cases the period distributions show outliers. These outliers could be related to real rotation frequencies or to false positives and could lead to an overestimate of $\Delta\Omega_{\text{phot}}$. In order to avoid this, we estimate P_{min} and P_{max} by taking the 5-th and the 95-th percentile of the distribution. Note that this rejection criterion is very cautious. Indeed, the percentage of measurements distant more than 3σ from the average period is less than 1-2% for the majority of our targets. In the right panel of Fig. 2, we show the true periods distribution obtained for ASAS J070030-7941.8 after beats rejection. In the picture, we report also the error bars associated with P_{min} and P_{max} . In Figs. 3-5 we plot also the distributions obtained for the stars ASAS J072851-3014.8, ASAS J084229-7903.9 and SWASP1 J101828.70-315002.8 taken as representative examples of our targets.

The total number of segments useful to measure the rotation period is different for each target. This number is a complex function of the time-series sampling and of the stellar rotation period. We divide our data in three quality groups according to the number of segments N in which a period with $FAP < 0.01$ is

measured. The group A includes stars with $N > 200$, the group B stars with N between 100 and 200 and the group C stars with $N < 100$.

3.3. False Alarm Probability estimate

We compute the False Alarm Probability associated with a given period P by using the Schwarzenberg-Czerny (1998) β distribution:

$$Pr[Z_{\text{max}} \leq z] = 1 - (1 - (1 - 2z)^{(N-3)/2})^M \quad (2)$$

where Z is the power related to P in the periodogram, N is the number of data-points and M the number of independent frequencies, i.e. the number of frequencies at which the periodogram powers are independent random variables. Unfortunately, in the case of an unevenly sampled time-series, M cannot be theoretically derived. In this work we use the value estimated by Distefano et al. (2012):

$$M = 1.8N_f/k \quad (3)$$

where N_f is the number of inspected frequencies and k is a factor introduced to take into account the periodogram oversampling and defined as $k = (1/T)/\delta\nu$ where T is the time interval spanned by the segment and $\delta\nu = 0.0001\text{d}^{-1}$ the frequency step adopted to sample the periodogram. Eq. (3) was derived by Distefano et al. (2012) by fitting empirical distributions of the peak powers Z as generated by Monte Carlo simulations. In our analysis we use only periods with $FAP \leq 0.01$.

3.4. Error estimate

The error associated with $\Delta\Omega_{\text{phot}}$ is given by

$$\sigma_{\Delta\Omega_{\text{phot}}}^2 = \sigma_{\Omega_{\text{max}}}^2 + \sigma_{\Omega_{\text{min}}}^2 \quad (4)$$

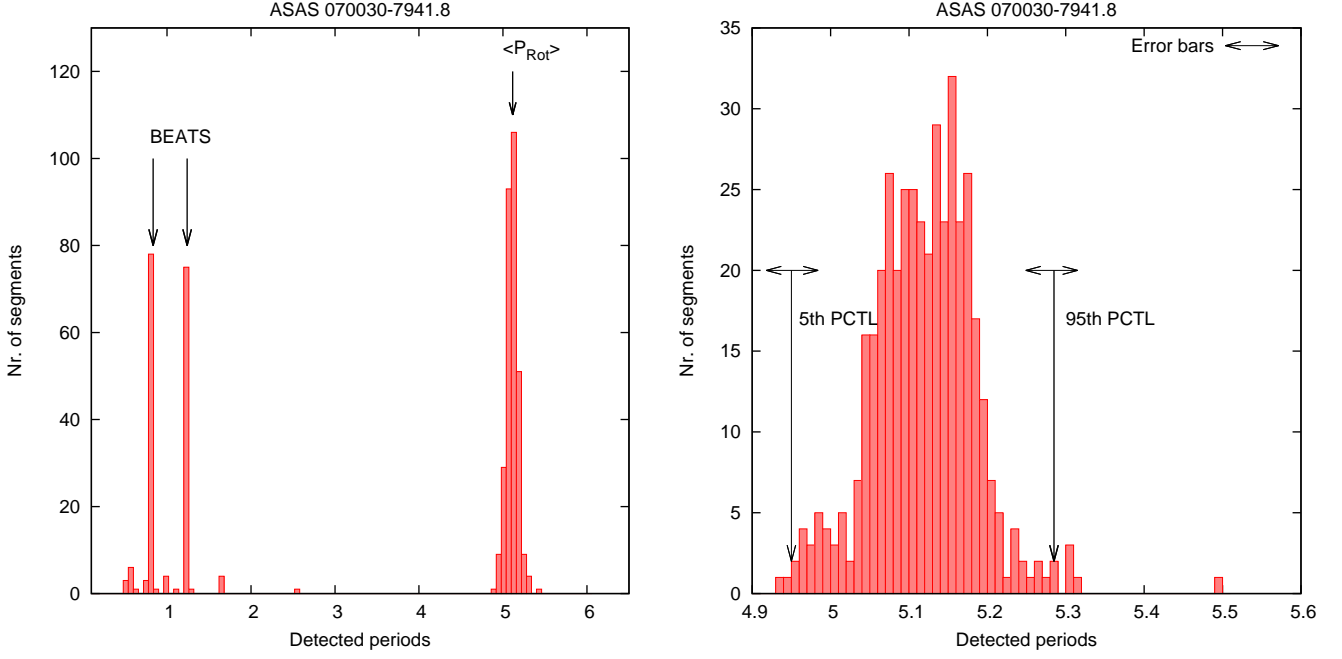


Fig. 2. *Left panel.* Distribution of detected periods for the star ASAS J070030-7941.8. The black continuous arrow marks the average rotation period $\langle P_{\text{Rot}} \rangle$. The black dotted arrows mark the beat periods. *Right panel.* Period distribution after beats rejections. P_{min} and P_{max} are estimated by taking the 5-th and the 95-th percentile of the distribution in order to avoid that $\Delta\Omega_{\text{phot}}$ computation is driven by outliers.

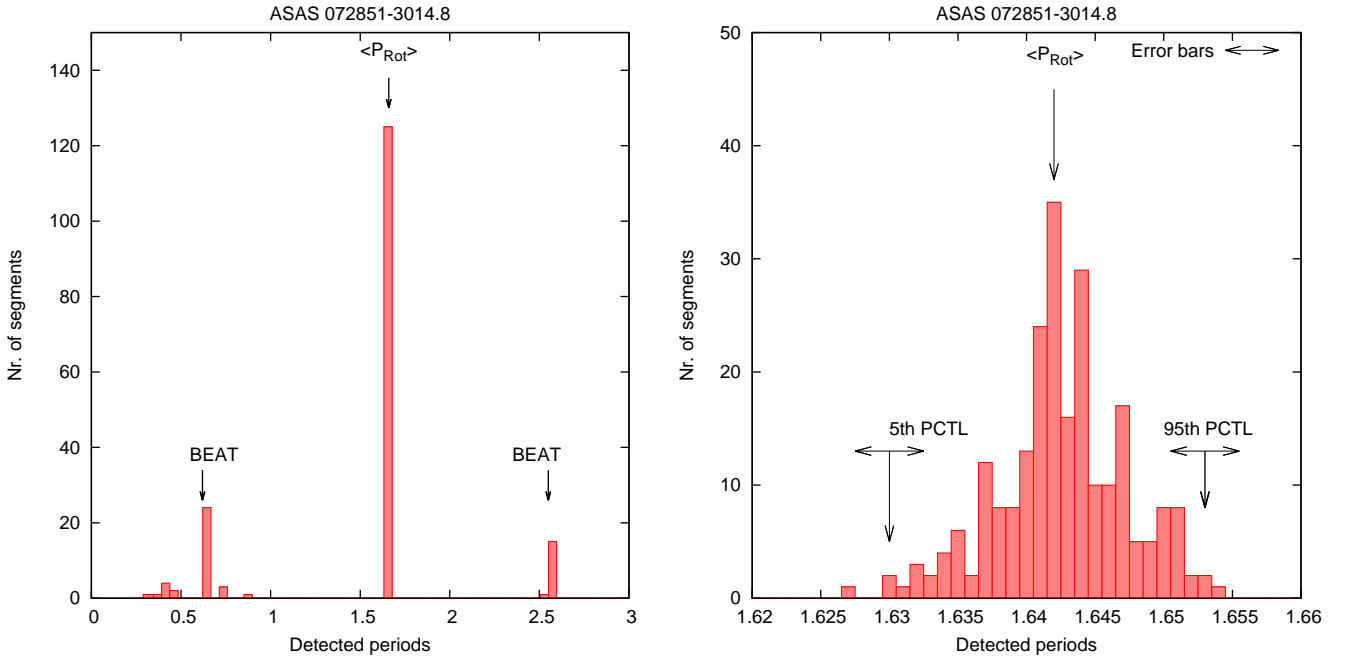


Fig. 3. The same of Fig. 2 for the star ASAS J072851-3014.8

where $\sigma_{\Omega_{\text{max}}} = 2\pi\sigma_{\nu_{\text{max}}}$ and $\sigma_{\Omega_{\text{min}}} = 2\pi\sigma_{\nu_{\text{min}}}$.

The error associated with the frequency detected by the Lomb-Scargle periodogram has two components. One component is due to the limited and discrete sampling of the signal whereas the other is due to the data noise. Kovacs (1981) estimates the error $\delta\nu_{\text{samp}}$ introduced by the sampling for a noise-free sinusoidal signal with frequency ν_0 and finds that this error is inversely correlated with $\nu_0 T^2$ where T is the interval spanned

by the time-series. Gilliland & Fisher (1985) show that the result found by Kovacs (1981) can be approximated by:

$$\delta\nu_{\text{samp}} = \frac{0.16}{\sqrt{2}\nu_0 T^2} \quad (5)$$

Kovacs (1981) derives this error for a signal uniformly sampled but the result can be applied also to unevenly sampled time-series. Kovacs (1981) makes also an estimate of the error caused

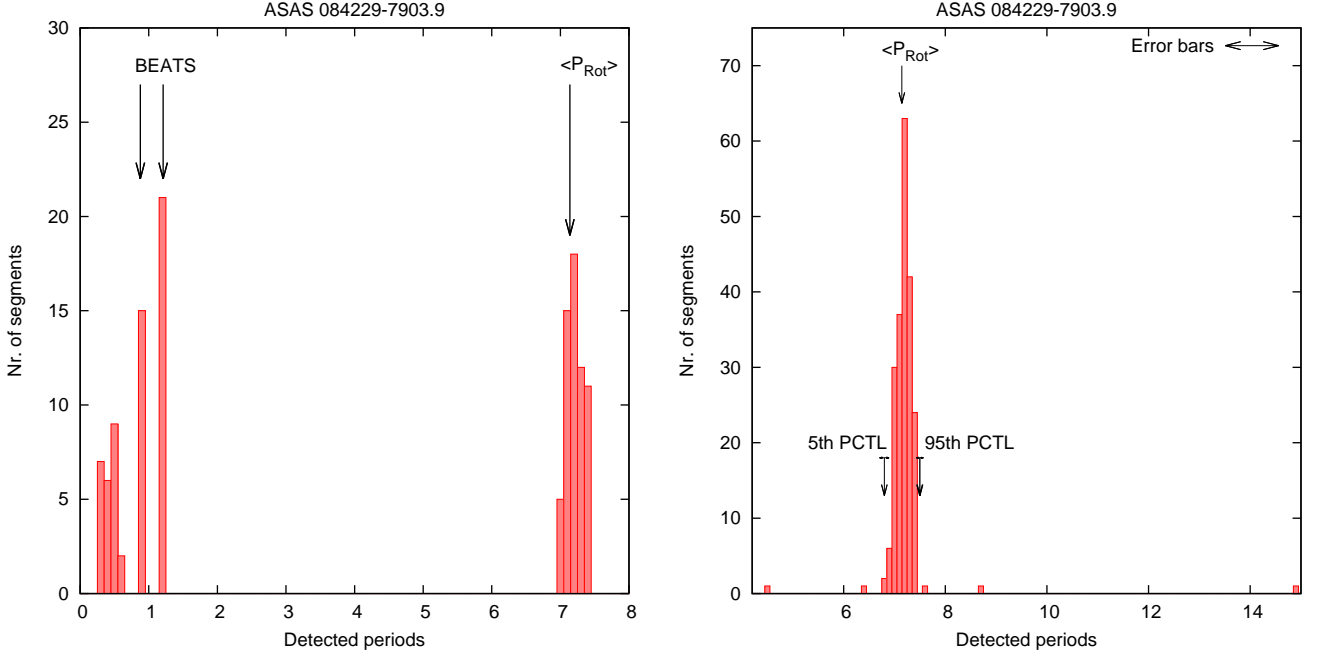


Fig. 4. The same of Fig. 2 for the star ASAS J084229-7903.0

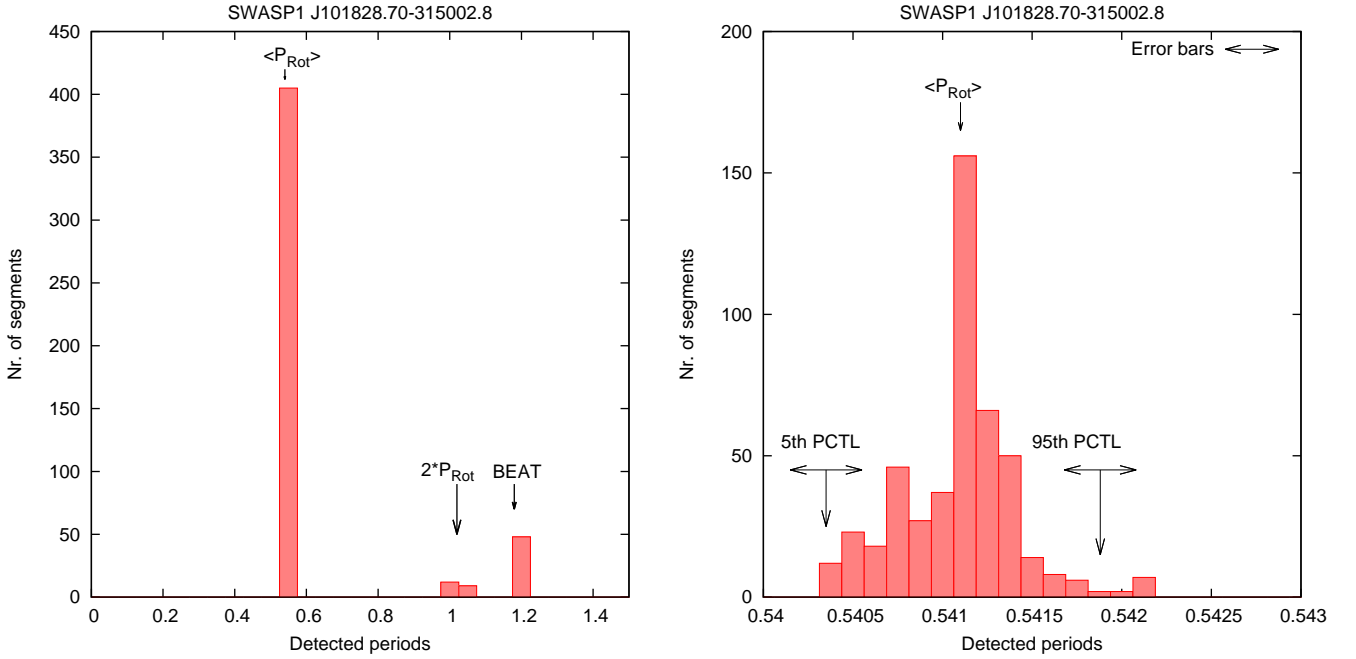


Fig. 5. The same of Fig. 2 for the star SWASP1 J101828.70-315002.8

by Gaussian white noise as :

$$\delta\nu_{\text{noise}} = \frac{3\sigma}{4\sqrt{N}\nu_0TA} \quad (6)$$

where σ is the standard deviation of the noise, N the number of time-series points and A the amplitude of the signal. Eq. (6) has been derived for a white Gaussian noise and can lead to an underestimation of the true error. In order to make a more realistic estimate of the error due to the data noise we use the following approach:

- we fit the data with a sinusoid;
- we compute the fit residuals in order to have an estimate of the data noise;
- we make 10000 permutations of the residuals and we construct 10000 synthetic time-series by adding the permuted residual to the sinusoid
- we run the period search algorithm on each synthetic time-series;
- we build the distribution of the detected frequencies and take the standard deviation of this distribution as an estimate of the error.

The error $\delta\nu_{\text{samp}}$ increases with the stellar rotation period (see Eq. 5). It is very small and ranges from 10^{-4} rad d $^{-1}$, for stars rotating in 0.5 d, to 0.006 rad d $^{-1}$ for stars rotating in 20 d (that is the highest rotation period detected in our target stars).

The error $\delta\nu_{\text{noise}}$ inferred from the simulation of synthetic time-series depends on different factors like the stellar magnitude, the amplitude of variability and the number of observations. It ranges between 0.003 rad d $^{-1}$ and 0.02 rad d $^{-1}$.

The final errors on $\Delta\Omega_{\text{phot}}$ measurements range between 0.005 and 0.025 rad d $^{-1}$.

3.5. Output of the analysis procedure

In Figs. 6-9 we show the typical output of our analysis for the stars ASAS J070030-7941.8, ASAS J072851-3014.8, ASAS J084229-7903.9 and SWASP1 J101828.70-315002.8

In the top panels we plot the rotation periods detected in the different segments vs. the mid-observation times of the same segments. In the central panels we plot the Interquartile Range (IQR) of the observed magnitudes, that can be regarded as an index of the variability amplitude, and in the bottom panels we plotted the median magnitude. The solid lines have been obtained by fitting the data with smoothing cubic splines and have been plotted in order to help the eye to follow the data trend. The period and the IQR seem to follow well defined patterns that suggest "cyclical" changes in the ARs configurations. These cyclical patterns will be investigated in a forthcoming work. In some segments, no significant periods have been detected. This can be ascribed to different reasons:

- the amplitude of the rotational modulation is of the same order of the photometric error and therefore it is too low to be detected;
- the ARs evolution occurs on a time scale comparable to or shorter than the length of the sliding window and therefore it masks the variability due to rotational modulation.

In Figs. 6-9 we also plot the results obtained by using 100-d and 150-d sliding windows for comparison. In principle, the use of the longer windows should give more precise measurements of the stellar rotation period as discussed in Sect. 3.4. In fact, the Equations shown in Sect. 3.4 are strictly valid only for a pure sinusoidal signal. In the case of solar-like variables, the intrinsic evolution of ARs tends to modify the amplitude and the phase of the rotational signal and the use of the longer windows does not improve the precision of the period measurements. Moreover, the use of a given window tends to filter out the variability phenomena occurring in a time-scale comparable with or shorter than the window length. This produces smoother curves and flattens the amplitude of the period variations. The use of a 50-d window is therefore more suitable to take into account the ARs evolution. Ideally, the length of the window should cover a small number of stellar rotations. Ferreira Lopes et al. (2015), for instance, suggest that long-term time-series of solar-like variables should be segmented in sub-series of length $5 \times P_{\text{Rot}}$ in order to limit the effects of ARs evolution. Unfortunately, a similar choice of the window length is unfeasible for the majority of our targets because of the sparse time-series sampling.

3.6. Comparison with other methods

In recent years, several methods have been developed to measure SDR in solar-like stars. Basically, these methods can be grouped in two classes. The first class comprises methods based on Doppler Imaging (see e.g. Donati et al. 1997;

Donati & Collier Cameron 1997; Strassmeier 2009; Waite et al. 2011) whereas the second comprises methods based on the analysis of photometric data (see e.g. Donahue et al. 1996; Reinhold et al. 2013; Lanza et al. 2014). The former are very effective in measuring SDR in fast rotating stars ($v \sin i \geq 15$ km s $^{-1}$) but cannot be successfully applied to slow rotators. The latter can be applied to slow rotators, but allow only the estimation of a lower limit for SDR. In this section, we discuss the main differences between our method and those employed by Waite et al. (2011) and Reinhold et al. (2013) taken as representative examples of the two classes.

3.6.1. Comparison with Zeeman Doppler Imaging

Waite et al. (2011) analyze spectro-polarimetric and photometric data, acquired during nine nights, to study the topology of the magnetic field and the differential rotation of HD 106506. They complement the information inferred from the Zeeman Doppler Imaging (ZDI) with the photometric data and derive an equatorial rotation period $P_0 = 1.39 \pm 0.01$ d and a photospheric shear $\Delta\Omega = 0.21 \pm 0.03$ rad d $^{-1}$. They also study the spots distribution on the stellar surface and find a large polar spot coupled with low and mid latitude features. In order to compare our detection method with that employed by Waite et al. (2011), we apply our analysis to the ASAS time-series of HD 106506

The shortest detected period is $P_{\text{min}} = 1.39$ d that is equal to the equatorial period found by Waite et al. (2011), while the longest period is $P_{\text{max}} = 1.445$ d. The shear inferred from P_{min} and P_{max} is $\Delta\Omega_{\text{phot}} = 0.17$ rad d $^{-1}$ that is about 20 per cent less than the value found by Waite et al. (2011). This difference is expected in view of the fact that the photometric analysis fails to detect the stellar rotation frequency at high latitudes because polar spots are always visible and do not induce an appreciable flux modulation.

3.6.2. Comparison with short-term photometry analysis

Reinhold et al. (2013) measure a lower limit of SDR for about 20000 late-type stars by analyzing the Q3 long-cadence photometric time-series collected by the Kepler mission. These time-series cover an interval of about 90 days and therefore are not suitable for segmentation. Reinhold et al. (2013) compute the Lomb-Scargle periodogram for the whole 90-d time-series and estimate the amplitude of SDR as

$$\Delta\Omega_{\text{phot}} = \Omega_1 - \Omega_2 \quad (7)$$

where $\Omega_1 = \frac{2\pi}{P_1}$, $\Omega_2 = \frac{2\pi}{P_2}$, and P_1 and P_2 are the two highest significant periods detected in the periodogram. Eq. (7) is based on the assumption that P_1 and P_2 are the rotation periods of two AR complexes located at different latitudes θ_1 and θ_2 . This kind of measurement has two drawbacks:

- the latitude range covered by θ_1 and θ_2 depends on the phase of the stellar magnetic cycle at which the time-series was collected. In fact, if a star has a solar-like cycle, the ARs gradually migrate from high latitudes (at the minimum of cycle) to the equator (at the maximum);
- it is based on the detection of multi periodicities in the same time-series and assumes that the secondary period P_2 is due to rotational modulation. However, as Aigrain et al. (2015) point out, the secondary peak in the Lomb-Scargle periodogram could be induced also by an intrinsic evolution of the ARs.

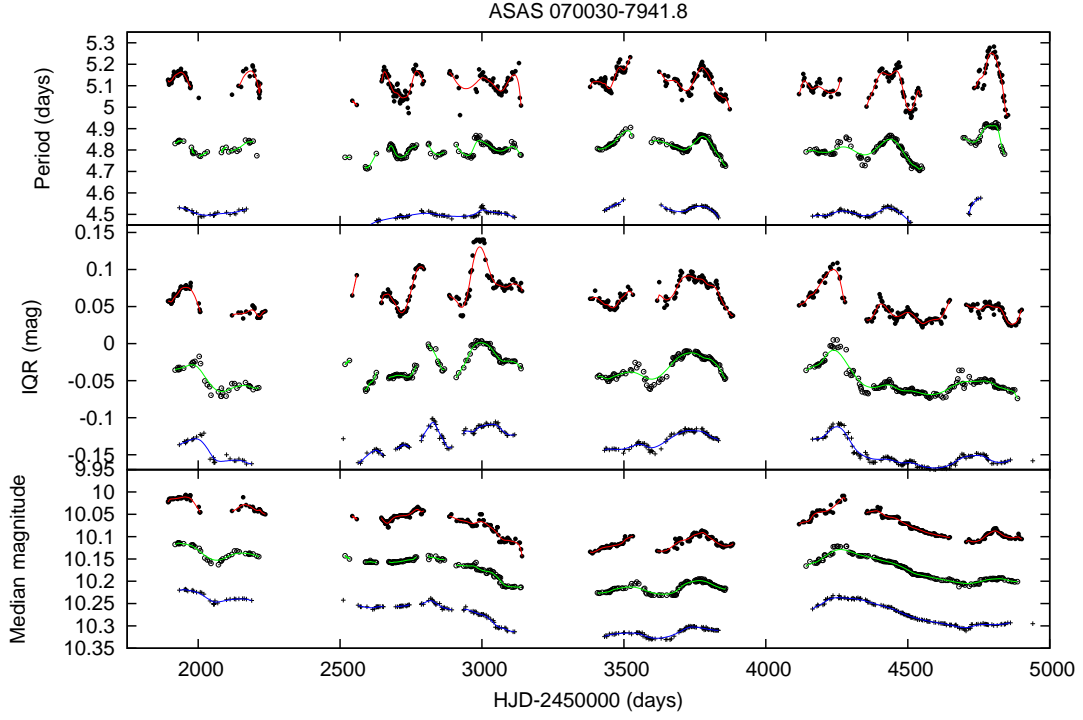


Fig. 6. The output of our analysis procedure in the case of the star with ASAS ID J070030-7941.8. The filled circles, the empty circles and the crosses are used to mark the results obtained with 50-d , 100-d and 150-d sliding windows, respectively. The results obtained with the 100-d and 150-d sliding window have been vertically shifted to make the plot clearer.

Top panel: rotation periods found in the different segments vs. time. Each point is located at the mid time of the corresponding segment. Mid panel: IQR measured in the different segments vs. time. Bottom panel: Median magnitude vs. time. The solid lines were obtained by fitting the data with smoothing cubic splines.

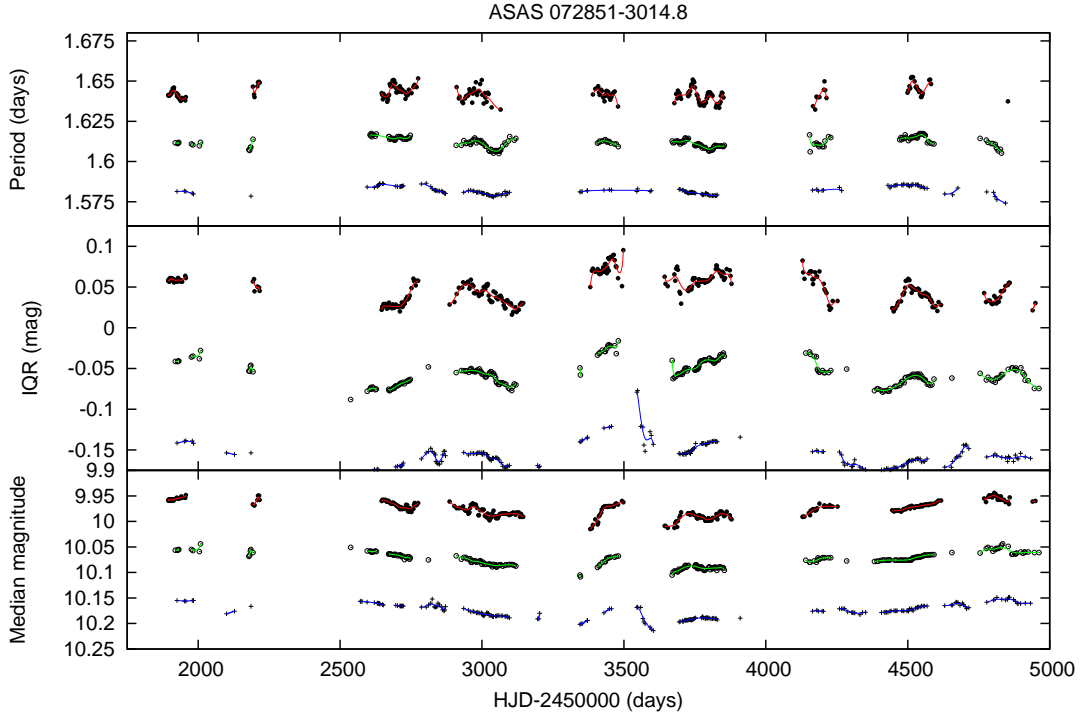


Fig. 7. The same of Fig. 6 for the star ASAS J072851-3014.8

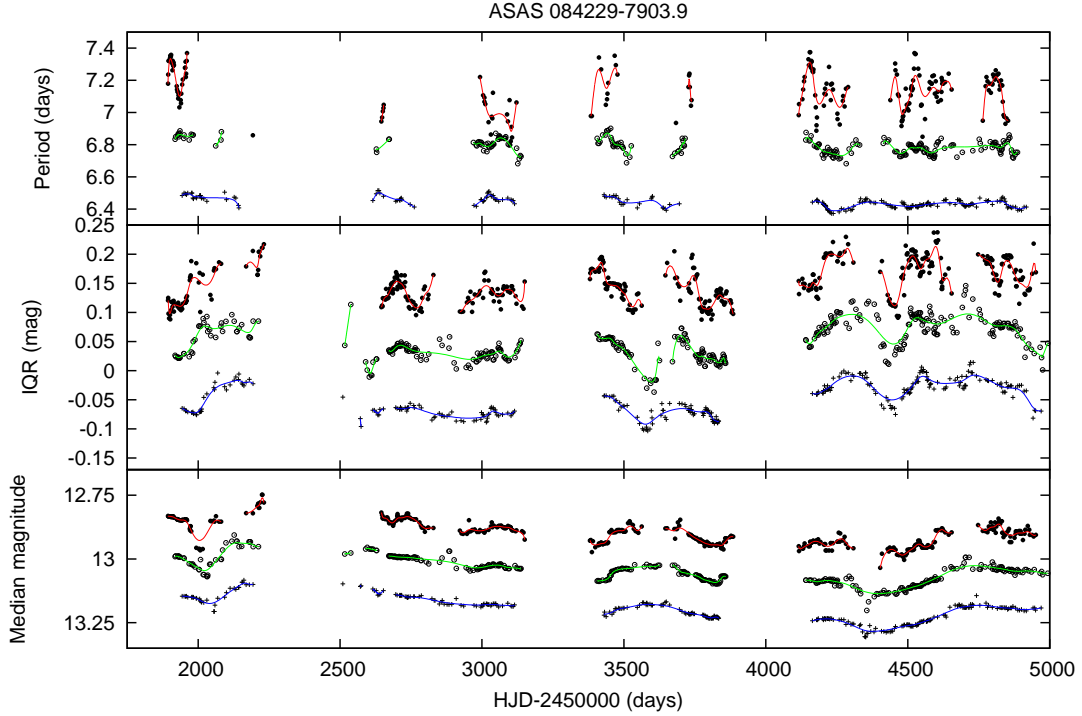


Fig. 8. The same of Fig. 6 for the star ASAS J0842.29-7903.9

The method employed here has two advantages over the technique used by Reinhold et al. (2013). First of all, it is based on the analysis of long-term photometry. The use of ASAS and Super-WASP time-series permits us to study our target stars over a time-scale comparable with the activity cycle duration and to track stellar rotation in a wider range of latitudes. This reduces the measurement bias due to the use of short-term photometry. The second advantage is that our method is not based on multiple periodicities, but searches for a drift in the primary period over the whole time-series. Aigrain et al. (2015) test different measurement methods on simulated light curves and show that the use of multiple peaks can sometimes fail in detecting and measuring SDR. The same authors point out that a more robust estimate of SDR can be done by searching for a drift in the mean period over an activity cycle.

4. Results

In Table 3 we report our $\Delta\Omega_{\text{phot}}$ measurements. If for a given source both ASAS and SuperWASP estimates are available, the highest $\Delta\Omega_{\text{phot}}$ value is reported. In the last column of the table we report a flag indicating whether the photometric shear has been computed with ASAS or SuperWASP data.

4.1. Correlation between SDR and global stellar parameters

We study how our $\Delta\Omega_{\text{phot}}$ measurements are related to the astrophysical parameters of our targets. The astrophysical parameters are inferred by using the infrared magnitudes M_J and M_H and the theoretical isochrones developed by Baraffe et al. (1998), Siess et al. (2000) and Spada et al. (2013). We use infrared magnitudes because the flux contrast between the spots and photosphere is lower in these wavelengths passbands. Hence these magnitudes are less affected by the variability induced by ro-

tational modulation in comparison with the optical magnitudes. For a given star, M_J and M_H are computed by adding the distance modulus DM to the J and H magnitudes reported in the 2MASS catalogue. The distance modulus is computed by using the stellar parallax or the distance reported in the literature. We do not apply any correction for reddening because the difference between the observed colors and those expected from the spectral type is within the photometric errors of the 2MASS photometry. The expected colors have been taken by the list compiled by Pecaut & Mamajek (2013) for the pre-main-sequence stars of different spectral types. In Table 4 we report the distance moduli and the inferred M_J and M_H magnitudes. In Table 5 we report, for each star, the mass and the effective temperature inferred by the comparison with the different models. We report also the global convective turnover time-scale τ_C inferred from the models of Spada et al. (2013) and the derived Rossby Number $R = \frac{P_{\text{rot}}}{\tau_C}$. The global convective turnover time-scale represents the characteristic time for the rise of a convective element through the stellar convection zone (see appendix A of Spada et al. 2013, for details on its computation).

4.1.1. Correlation between SDR and stellar temperature

In Fig. 10 we plot $\Delta\Omega_{\text{phot}}$ vs. the color index $B - V$ of our targets. Different symbols are used to mark stars belonging to different associations. Though the data are quite scattered, we note a general trend with SDR amplitude increasing toward bluest colors. The scatter can be ascribed to two different reasons. First of all, it is related to the intrinsic limitations of our measurement method that allows only the detection of a lower limit for SDR (see discussion in Sect. 3). The second reason is that the plot mixes stars with different ages and rotation periods. Despite the scatter, the trend shown in the picture is in agreement with the theoretical models developed by Kitchatinov & Rüdiger (1999)

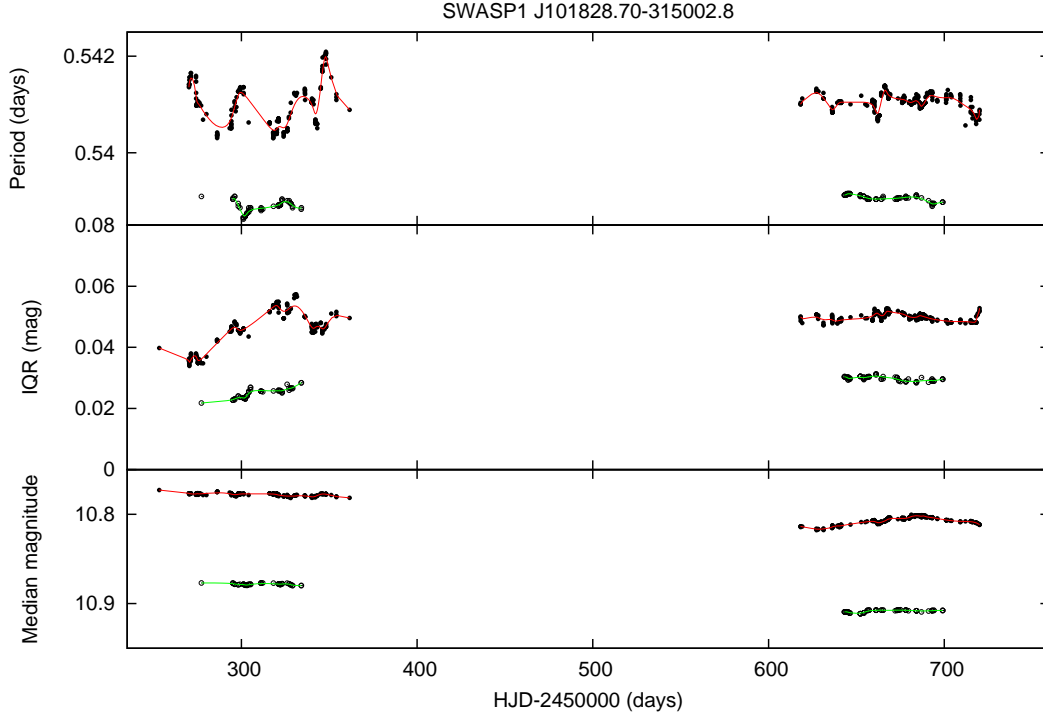


Fig. 9. The same of Fig. 6 for the star SWASP1 J101828.70-315002.8. The analysis with a 150-d sliding window has not been performed in this case because the two observation seasons span are not long enough.

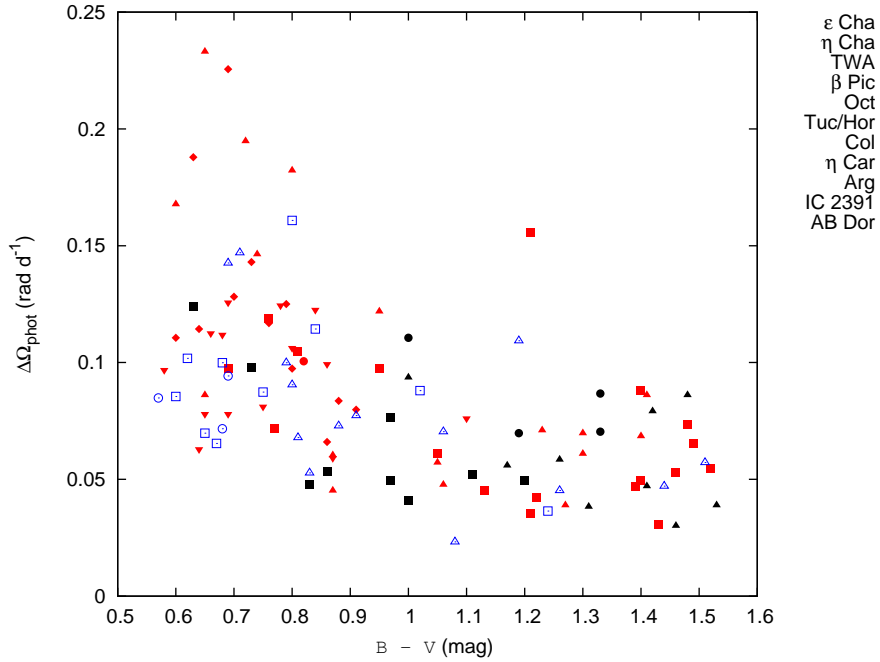


Fig. 10. The quantity $\Delta\Omega_{\text{phot}}$ measured in the present work vs. the color index $B - V$. $\Delta\Omega_{\text{phot}}$ increases toward bluest stars. The different symbols are used to mark stars belonging to different associations.

and Küker & Rüdiger (2011). In fact, in these models, the amplitude of stellar SDR is inversely correlated with the depth of the convective zone and, therefore, it increases toward higher temperatures.

In order to make a quantitative comparison between our results and those predicted by Küker & Rüdiger (2011), we study the correlation between $\Delta\Omega_{\text{phot}}$ and the stellar temperature.

In Fig. 11, we plot $\Delta\Omega_{\text{phot}}$ vs. the effective temperature T_{eff} inferred from the Siess et al. (2000) isochrones. The model of Küker & Rüdiger (2011) predicts the relationship $\Delta\Omega =$

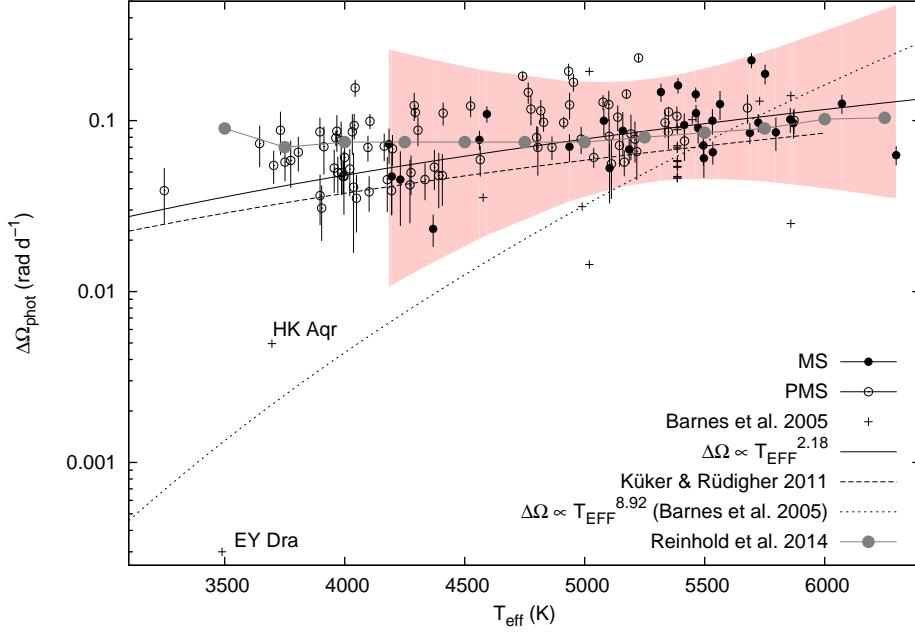


Fig. 11. $\Delta\Omega_{\text{phot}}$ vs. the effective temperature T_{eff} . The black bullets mark the values measured in the present work. The filled bullets mark stars that have reached ZAMS and the empty bullets mark stars that are still contracting. The black crosses mark the data reported in Barnes et al. (2005). The continuous and the dotted line depict the power law inferred in the present work and that inferred in Barnes et al. (2005), respectively. The dashed line indicates the power law predicted by the theoretical model of Küker & Rüdiger (2011). The T_{eff} values have been inferred from the Siess et al. (2000) models. The shaded area represents the uncertainty in our power law fitting. Large gray bullets and grey line represents the results of Reinhold et al. (2013)

$0.071(\frac{T_{\text{eff}}}{5500})^2$ for ZAMS stars with $T_{\text{eff}} \leq 6000\text{K}$. Our targets comprise PMS stars that are still contracting and stars recently settled on MS. We select MS stars by comparing the masses and ages of our targets with the values tabulated by Siess et al. (2000) for the ZAMS stars. We fit our ZAMS data with a power-law and we find $\Delta\Omega_{\text{phot}} = 0.09(\frac{T_{\text{eff}}}{5500})^{2.18 \pm 0.65}$.

The use of Baraffe et al. (1998) or Spada et al. (2013) isochrones does not change significantly this result. The power-laws obtained with the two models are $\Delta\Omega_{\text{phot}} = 0.105(\frac{T_{\text{eff}}}{5500})^{2.06 \pm 0.7}$ and $\Delta\Omega_{\text{phot}} = 0.09(\frac{T_{\text{eff}}}{5500})^{2.6 \pm 0.6}$, respectively. Though the data are quite scattered, the exponents of the theoretical and fitted power laws are in good agreement with each other. However, the two curves exhibit a small offset of about 0.01 rad d^{-1} and our measurements are, on average, higher than the values predicted by Küker & Rüdiger (2011). We remind that our analysis tends to underestimate SDR, hence the shift between theoretical and real values could be more pronounced than that shown in the picture. In Fig. 11, we also plot the results of Reinhold et al. (2013) and those from Barnes et al. (2005) for comparison. We plot the median $\Delta\Omega_{\text{phot}}$ values found by Reinhold et al. (2013) in different T_{eff} bins. These median values fall inside the 95% confidence region of our fitted power law. Hence the two works can be considered in agreement. Note however that the trend found by Reinhold et al. (2013) is more flattened than the power law found here and that predicted by Küker & Rüdiger (2011). This discrepancy could be due to the fact that Reinhold et al. (2013) mix stars with different ages and with a wider range of rotation periods.

Barnes et al. (2005) analyze a sample of ten young late-type stars and find the relationship $\Delta\Omega \propto T_{\text{eff}}^{8.92}$. The targets investigated by Barnes et al. (2005) comprises PMS stars and stars recently settled in the ZAMS. Their power law is much more

steep than that predicted by Küker & Rüdiger (2011) and in disagreement with the trend of our PMS and ZAMS data. Hence our targets do not confirm Barnes et al. (2005) finding.

4.1.2. Correlation between SDR and global convective turnover time-scale

The stars analyzed in the present work span the age range 4–95 Myr. During this time interval, the stellar structure evolves from a fully convective structure to a radiative core plus a convective envelope. Hence, in our sample, stars with the same effective temperature can have very different structures depending on their age and mass. In this age range, the convective turn-over time scale τ_C could be a more convenient parameter for investigating the relationship between the SDR and the stellar structure. Indeed τ_C is proportional to the depth of the convective zone and is more representative of the stellar structure than the effective temperature.

In Fig. 12 we plot $\Delta\Omega_{\text{phot}}$ vs. τ_C . $\Delta\Omega_{\text{phot}}$ increases toward shorter τ_C values. Hence $\Delta\Omega_{\text{phot}}$ increases as the depth of the convective envelope decreases. This result is in agreement with the theoretical models of Kitchatinov & Rüdiger (1999), Küker & Rüdiger (2011) and Küker et al. (2011). We fit a power law to our data and we find $\Delta\Omega_{\text{phot}} \propto \tau_C^{-0.25 \pm 0.04}$ (red line in the picture). Though the data exhibit a clear trend, they are broadly spread around the fitted power law. This spread is partly due to the limitations of our measurement method and partly due to the fact that the plot mixes stars with different rotation periods.

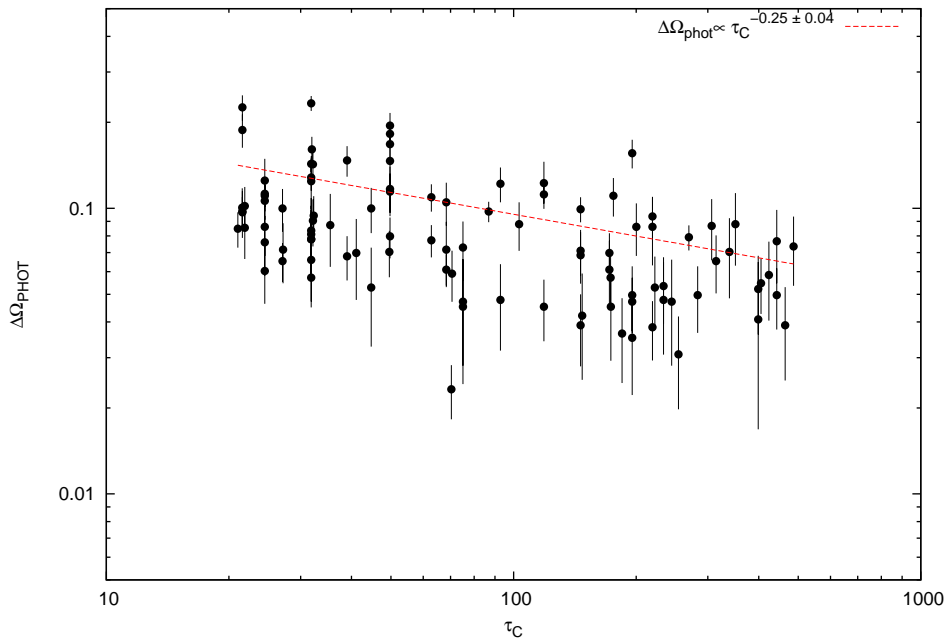


Fig. 12. $\Delta\Omega_{\text{phot}}$ vs. the convective turn-over time-scale τ_C .

4.1.3. Correlation between SDR and the rotation period

In the top panel of Fig. 13 we plot $\Delta\Omega_{\text{phot}}$ vs. the rotation period P_{rot} . In this case, the data do not follow a well defined trend and cannot be reproduced by a power law. However, SDR seems somehow related to the stellar rotation period. In fact, the highest values of $\Delta\Omega_{\text{phot}}$ correspond to P_{rot} between 0.7 and 5 d. Küker & Rüdiger (2011) study in detail how SDR depends on rotation period in ZAMS stars. They compute differential rotation for stars with different masses and periods and derive a set of "rotational tracks". Each track shows how $\Delta\Omega$ depends on rotation period for a fixed stellar mass. In the bottom panel of Fig. 13, we plot the rotational tracks derived by Küker & Rüdiger (2011) for stars with 0.5, 0.7, 0.9 and 1.1 M_{\odot} . According to these tracks, SDR is almost independent of the stellar rotation period and is more influenced by the stellar mass. We over-plot our results on the tracks for comparison. We report only stars that have reached the ZAMS because the tracks have been computed for ZAMS stars. The masses of these targets cover the range 0.6 – 1.35 M_{\odot} . The circles size is proportional to the stellar mass. Our results show a trend that partly resembles the rotational tracks. Indeed, the less massive stars exhibit on average a lower SDR. However, for stars with P_{rot} between 0.7 and 2 d, there is a strong discrepancy with the model predictions. This suggests that the stellar mass cannot be the main parameter on which SDR depends as claimed by Küker & Rüdiger (2011) and that stellar rotation period plays a key role too.

4.1.4. Correlation between SDR and stellar age

The stellar associations studied in the present work span an age range between 4 and 95 Myr. Hence our sample includes stars that are in the first phases of the PMS stage and stars that are approaching or recently settled on the MS. Our results are therefore useful to investigate how SDR evolves in time during the PMS stage. In the top panel of Fig. 14, we display the measured values of $\Delta\Omega_{\text{phot}}$ vs. the stellar age. The median $\Delta\Omega_{\text{phot}}$ increases

between 4 and 30 Myr and then decreases and approaches the current solar value at 95 Myr. The scatter of the data is partly due to the intrinsic limitations related to our methodology and partly to the fact that the picture mixes stars with different masses and rotation periods. In the bottom panel of Fig. 14 we report only stars with masses between 0.85 and 1.15 M_{\odot} and we investigate how $\Delta\Omega_{\text{phot}}$ evolves in a young Sun. The median $\Delta\Omega_{\text{phot}}$ is constant in the first 17 Myr, then it significantly increases and, at 30 Myr, its value is about twice the initial value. Between 30 and 95 Myr $\Delta\Omega_{\text{phot}}$ remains almost constant. Küker & Stix (2001) model SDR evolution in the Sun. They develop four theoretical models for the Sun at 3, 10 and 31 Myr and for the present Sun. In their models $\Delta\Omega$ is inversely correlated to the depth of convective zone. This implies that $\Delta\Omega$ increases between 3 and 31 Myr. At 3 Myr, the Sun has a fully convective structure and a small SDR. As the Sun evolves in time, a radiative core grows, the depth of the convective zone decreases and $\Delta\Omega$ increases. Küker & Stix (2001) do not find a significant difference between the 31 Myr and the present Sun models. Hence, according to their work, the Sun should have reached its current $\Delta\Omega$ value at about 30 Myr. Also in this case, our results agree only qualitatively with the model prediction. Indeed the median $\Delta\Omega_{\text{phot}}$ values increase between 4 and 30 Myr, but they are systematically higher than those predicted by Küker & Stix (2001). Note that, though these young stars exhibit a SDR greater than the solar one, they can be regarded as solid body rotators because they rotate faster than the present Sun and have a low relative shear

$$\alpha = \frac{\Delta\Omega}{\Omega_{\text{eq}}}$$

5. Discussion

In the last section we showed that our results are qualitatively in agreement with the models developed by Kitchatinov & Rüdiger (1999) and Küker & Rüdiger (2011). However our $\Delta\Omega_{\text{phot}}$ measurements are often higher than the values predicted by the same models (see Fig. 11 and 13), especially in stars with periods be-

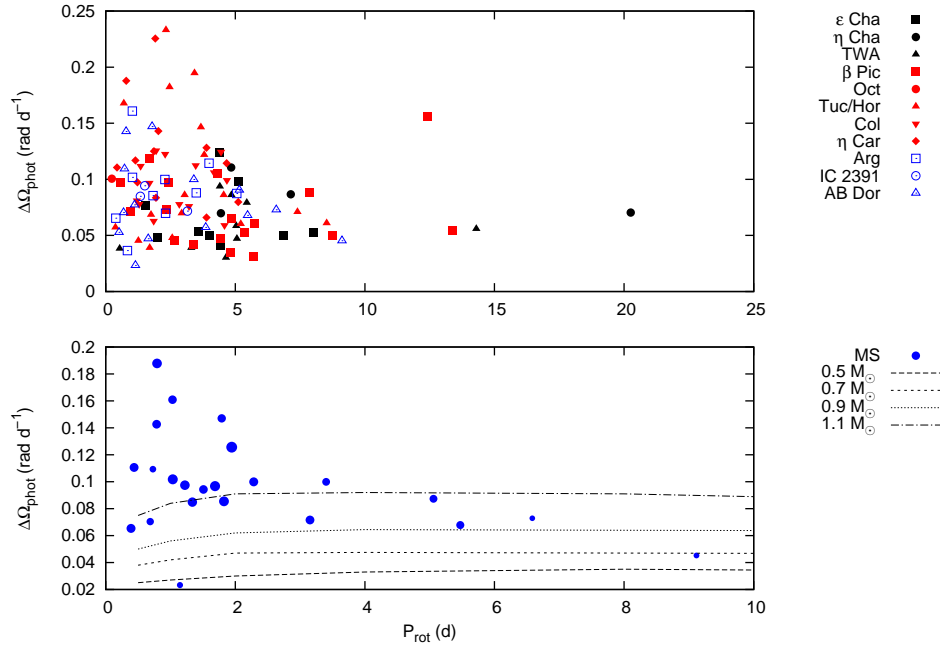


Fig. 13. Top panel: $\Delta\Omega_{\text{phot}}$ vs. the stellar rotation period P_{rot} . The highest $\Delta\Omega_{\text{phot}}$ values have been measured in stars with $P_{\text{rot}} \leq 5$ d. Bottom panel: the same plot restricted to the MS stars. The symbol sizes are proportional to the stellar masses that range between 0.6 and $1.35 M_{\odot}$. The black lines are the rotational tracks derived by Küker & Rüdiger (2011) for stars of 0.5 , 0.7 , 0.9 and $1.1 M_{\odot}$ as labelled, respectively.

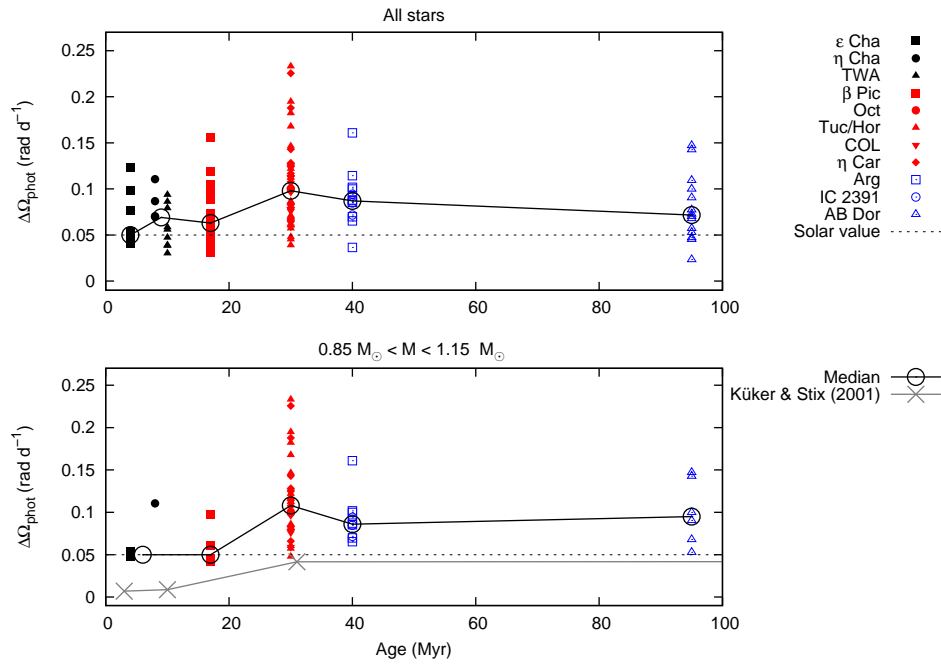


Fig. 14. Top panel: $\Delta\Omega_{\text{phot}}$ vs. the stellar age. The empty circles indicate the median $\Delta\Omega_{\text{phot}}$ values measured at different ages (note that the members of η Cha have been grouped with the members of TWA). The black continuous line connects the median $\Delta\Omega_{\text{phot}}$ values and the dotted line marks the present solar shear for comparison. Bottom panel: the same plot restricted to stars with mass between 0.9 and $1.1 M_{\odot}$. The grey crosses mark the rotational shear for the Sun at different ages as predicted by Küker & Stix (2001)

tween 0.7 and 2 d. Such a disagreement between $\Delta\Omega$ values and models predictions has been already noticed and discussed by Marsden et al. (2006). These authors measured an absolute shear $\Delta\Omega = 0.4 \text{ rad d}^{-1}$ for the G0 star HD 171488. This value is significantly higher than those measured for the G dwarfs R58 and LQ Lup, that are $\Delta\Omega = 0.138 \text{ rad d}^{-1}$ and $\Delta\Omega = 0.12 \text{ rad d}^{-1}$,

respectively (Marsden et al. 2005; Donati et al. 2000). According to the models, the three stars should have about the same rotational shear because the stellar temperature is the main parameter on which $\Delta\Omega$ depends. Küker et al. (2011) were not able to find an explanation about this discrepancy and questioned the reliability of the $\Delta\Omega$ measurement for HD 171488. How-

ever Jeffers & Donati (2008) made an independent measurement and found $\Delta\Omega = 0.5 \text{ rad d}^{-1}$. The main difference between HD 171488 and the other two stars lies in the rotation period. Indeed, HD 171488 has a rotation period of 1.31 d, whereas the other two stars have a rotation period of 0.5 and 0.3 days respectively.

As a matter of fact, the rotational tracks computed by Küker & Rüdiger (2011) predict that SDR amplitude slightly increases with the period in the range 0.3-2 d (see bottom panel of Fig. 13) but this increment is too small to explain the SDR amplitude of HD 171488. The high differential rotation found in HD 171488 and in our targets, with periods between 0.7 and 2 d, suggest that the dependence on the rotation period could be more pronounced than models prediction.

A stronger dependence on the stellar rotation rate could also explain the discrepancy between the power law found by Barnes et al. (2005) and that found in the present work (see Fig 11). Indeed, the high steepness of the power law found by Barnes et al. (2005) is due to the M1V stars HK Aqr and EY Dra for which the authors measure very low SDR values i.e. 0.005 and 0.0003 rad d^{-1} , respectively. The M1V stars of our sample have in comparison higher $\Delta\Omega_{\text{phot}}$ values. However, we point out that HK Aqr and EY Dra rotate in about 0.5 days whereas the M1V stars investigated here have rotation periods between 1.5 and 5.5 days. Thus the difference between HK Aqr, EY Dra and the M1V stars investigated here could be due to the different rotation periods.

The models developed by Küker & Rüdiger (2011) are based on the so called Λ effect. In these models the main driver of the differential rotation is the non-diffusive term of the Reynolds stress induced by the interaction between the Coriolis force and the convective motions. As noticed by Gastine et al. (2014), these models depend on free parameters like the turbulent viscosity coefficients. A different choice of these parameters could maybe lead to a stronger dependence on stellar rotation rate. Gastine et al. (2014) developed a model based on a 3D hydrodynamical code where the Reynolds stresses do not need to be parametrized. In this model, the main parameter on which $\Delta\Omega$ depends is the Rossby number $Ro = \frac{P_{\text{rot}}}{\tau_c}$ where P_{rot} is the stellar rotation period and τ_c is the convective turnover timescale. If $Ro < 1$, that is the case of our targets, the Coriolis force dominates the buoyancy and the star tends to rotate as a solid-body. As Ro increases the Coriolis force becomes less important and the value of differential rotation increases. For $Ro > 1$ the buoyancy dominates on Coriolis force and the SDR becomes anti solar. In Fig. 15 we plot $\Delta\Omega_{\text{phot}}$ vs. the Rossby Number computed in Sec. 3. The plot is quite scattered, but the trend of $\Delta\Omega_{\text{phot}}$ seems to confirm the prediction of Gastine et al. (2014). In the bottom panel of the Fig. 15, we report the relative shear α_{phot} vs. the Rossby number. The trend and the range of α_{phot} values are very similar to that predicted by Gastine et al. (2014) and shown in the Fig. 2 of their work.

6. Conclusions

We investigate the correlation between the amplitude of SDR and global stellar parameters in members of young loose stellar associations. We measure the quantities $\Delta\Omega_{\text{phot}}$ and α_{phot} for 111 stars by processing long-term photometric time-series. These quantities are lower limits to the absolute and to the relative surface rotational shear, respectively. Our analysis leads to the following results:

- $\Delta\Omega_{\text{phot}}$ increases with the effective temperature T_{eff} following the power law $\Delta\Omega_{\text{phot}} \propto T_{\text{eff}}^{2.18 \pm 0.65}$ in MS stars. This power law is very close to that predicted by Küker & Rüdiger (2011) (i.e. $\Delta\Omega \propto T_{\text{eff}}^2$);
- the PMS stars of our sample show a trend very similar to that exhibited by MS stars. Thus, the power law $\Delta\Omega \propto T_{\text{eff}}^{8.6}$ found by Barnes et al. (2005) for PMS and ZAMS stars is not confirmed by our measurements;
- $\Delta\Omega_{\text{phot}}$ increases with decreasing convective turnover time-scale τ_c according to the power law $\Delta\Omega_{\text{phot}} \propto \tau_c^{-0.25 \pm 0.4}$;
- our $\Delta\Omega_{\text{phot}}$ measurements are systematically higher than the values predicted by Küker & Rüdiger (2011). This discrepancy is particularly large in stars with a rotation period between 0.7 and 2 d and suggests that the dependence on the rotation period could be stronger than the model prediction;
- we investigate the time evolution of $\Delta\Omega_{\text{phot}}$ for a $1 M_{\odot}$ stars and find that $\Delta\Omega_{\text{phot}}$ increases with the stellar age in the first 30 Myr. This is consistent with the theoretical models that predict a low degree of differential rotation for fully convective stars;
- $\Delta\Omega_{\text{phot}}$ and α_{phot} increase with the Rossby number Ro in agreement with the theoretical model developed by Gastine et al. (2014).

Acknowledgements. The authors are grateful to Rainer Arlt and to the anonymous referee for helpful comments and suggestions.

References

- Aigrain, S., Llama, J., Ceillier, T., et al. 2015, MNRAS, 450, 3211
 Baraffe, I., Chabrier, G., Allard, F., & Hauschildt, P. H. 1998, A&A, 337, 403
 Barnes, J. R., Collier Cameron, A., Donati, J.-F., et al. 2005, MNRAS, 357, L1
 Barrado Y Navascués, D. 2006, A&A, 459, 511
 Barrado y Navascués, D., Stauffer, J. R., & Jayawardhana, R. 2004, ApJ, 614, 386
 Borucki, W. J., Koch, D., Basri, G., et al. 2010, Science, 327, 977
 Brandenburg, A., Moss, D., Rüdiger, G., & Tuominen, I. 1991, Geophysical and Astrophysical Fluid Dynamics, 61, 179
 Butters, O. W., West, R. G., Anderson, D. R., et al. 2010, A&A, 520, L10
 Collier Cameron, A. 2007, Astronomische Nachrichten, 328, 1030
 De Silva, G. M., D'Orazi, V., Melo, C., et al. 2013, MNRAS, 431, 1005
 Distefano, E., Lanzafame, A. C., Lanza, A. F., et al. 2012, MNRAS, 421, 2774
 Donahue, R. A., Dobson, A. K., & Baliunas, S. L. 1997a, Sol. Phys.
 Donahue, R. A., Dobson, A. K., & Baliunas, S. L. 1997b, Sol. Phys.
 Donahue, R. A., Saar, S. H., & Baliunas, S. L. 1996, ApJ, 466, 384
 Donati, J.-F. & Collier Cameron, A. 1997, MNRAS, 291, 1
 Donati, J.-F., Mengel, M., Carter, B. D., et al. 2000, MNRAS, 316, 699
 Donati, J.-F., Semel, M., Carter, B. D., Rees, D. E., & Collier Cameron, A. 1997, MNRAS, 291, 658
 Feigelson, E. D., Lawson, W. A., & Garmire, G. P. 2003, ApJ, 599, 1207
 Ferreira Lopes, C. E., Leão, I. C., de Freitas, D. B., et al. 2015, A&A, 583, A134
 Gastine, T., Yadav, R. K., Morin, J., Reiners, A., & Wicht, J. 2014, MNRAS, 438, L76
 Gilliland, R. L. & Fisher, R. 1985, PASP, 97, 285
 Hussain, G. A. J. 2002, Astronomische Nachrichten, 323, 349
 Jeffers, S. V. & Donati, J.-F. 2008, MNRAS, 390, 635
 Kitchatinov, L. L. & Rüdiger, G. 1999, A&A, 344, 911
 Kovacs, G. 1981, Ap&SS, 78, 175
 Küker, M. & Rüdiger, G. 2011, Astronomische Nachrichten, 332, 933
 Küker, M., Rüdiger, G., & Kitchatinov, L. L. 2011, A&A, 530, A48
 Küker, M. & Stix, M. 2001, A&A, 366, 668
 Lanza, A. F., Das Chagas, M. L., & De Medeiros, J. R. 2014, A&A, 564, A50
 Lanza, A. F., Rodonó, M., & Pagano, I. 2004, A&A, 425, 707
 Lanza, A. F., Rodonó, M., Pagano, I., Barge, P., & A., L. 2003, A&A, 403, 1135
 Lawson, W. & Feigelson, E. D. 2001, in Astronomical Society of the Pacific Conference Series, Vol. 243, From Darkness to Light: Origin and Evolution of Young Stellar Clusters, ed. T. Montmerle & P. André, 591
 López-Santiago, J., Montes, D., Crespo-Chacón, I., & Fernández-Figueroa, M. J. 2006, ApJ, 643, 1160
 Luhman, K. L., Stauffer, J. R., & Mamajek, E. E. 2005, ApJ, 628, L69
 Makarov, V. V. 2007, ApJS, 169, 105

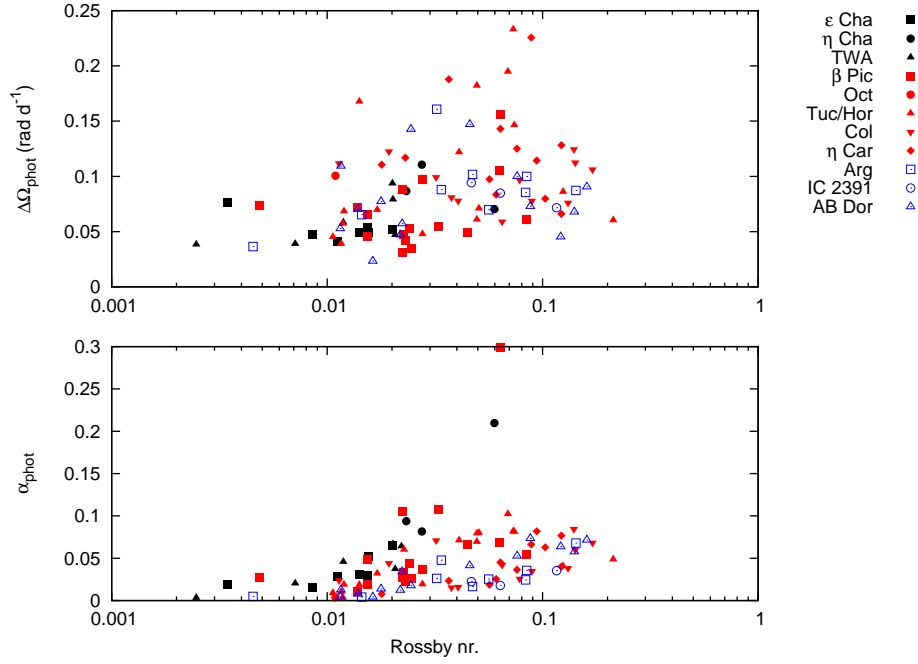


Fig. 15. Top panel: the absolute shear $\Delta\Omega$ vs. the Rossby number Ro . Bottom panel: the relative shear α vs. Ro . $\Delta\Omega$ and α increase toward higher Ro values. This trend is in agreement with the model developed by Gastine et al. (2014).

- Mamajek, E. E., Lawson, W. A., & Feigelson, E. D. 1999, *ApJ*, 516, L77
Mamajek, E. E., Lawson, W. A., & Feigelson, E. D. 2000, *ApJ*, 544, 356
Marsden, S. C., Carter, B. D., & Donati, J.-F. 2005, 560, 799
Marsden, S. C., Donati, J.-F., Semel, M., Petit, P., & Carter, B. D. 2006, *MNRAS*, 370, 468
Mentuch, E., Brandeker, A., van Kerkwijk, M. H., Jayawardhana, R., & Hauschildt, P. H. 2008, *ApJ*, 689, 1127
Messina, S., Desidera, S., Lanzafame, A. C., Turatto, M., & Guinan, E. F. 2011, *A&A*, 532, A10
Messina, S., Desidera, S., Turatto, M., Lanzafame, A. C., & Guinan, E. F. 2010, *A&A*, 520, A15
Messina, S. & Guinan, E. F. 2003, *A&A*, 409, 1017
Moss, D. & Brandenburg, A. 1995, *Geophysical and Astrophysical Fluid Dynamics*, 80, 229
Murphy, S. J. & Lawson, W. A. 2015, *MNRAS*, 447, 1267
Murphy, S. J., Lawson, W. A., & Bessell, M. S. 2013, *MNRAS*, 435, 1325
Parker, E. N. 1955, *ApJ*, 122, 293
Pecaut, M. J. & Mamajek, E. E. 2013, *ApJS*, 208, 9
Perryman, M. A. C., Lindegren, L., Kovalevsky, J., et al. 1997, *A&A*, 323, L49
Pojmanski, G. 1997, *Acta Astronomica*, 47, 467
Pollacco, D. L., Skillen, I., Collier Cameron, A., et al. 2006, *PASP*, 118, 1407
Reinhold, T., Reiners, A., & Basri, G. 2013, *A&A*, 560, A4
Schwarzenberg-Czerny, A. 1998, *MNRAS*, 301, 831
Siess, L., Dufour, E., & Forestini, M. 2000, *A&A*, 358, 593
Song, I., Zuckerman, B., & Bessell, M. S. 2003, *ApJ*, 599, 342
Spada, F., Demarque, P., Kim, Y.-C., & Sills, A. 2013, *ApJ*, 776, 87
Strassmeier, K. G. 2009, *A&A Rev.*, 17, 251
Tamuz, O., Mazeh, T., & Zucker, S. 2005, *MNRAS*, 356, 1466
Torres, C. A. O., Quast, G. R., da Silva, L., et al. 2006, *A&A*, 460, 695
Torres, C. A. O., Quast, G. R., de La Reza, R., da Silva, L., & Melo, C. H. F. 2001, in *Astronomical Society of the Pacific Conference Series*, Vol. 244, *Young Stars Near Earth: Progress and Prospects*, ed. R. Jayawardhana & T. Greene, 43
Torres, C. A. O., Quast, G. R., Melo, C. H. F., & Sterzik, M. F. 2008, *Young Nearby Loose Associations*, ed. B. Reipurth, 757
Waite, I. A., Marsden, S. C., Carter, B. D., et al. 2011, *MNRAS*, 413, 1949
Webb, R. A., Zuckerman, B., Platais, I., et al. 1999, *ApJ*, 512, L63
Zuckerman, B. & Webb, R. A. 2000, *ApJ*, 535, 959

Table 2. List of the targets investigated in the present work

Target ID	Target Name	Assoc.	$B - V$ (mag)	Sp. Type
ASAS J001353-7441.3	HIP 1113	TUC/HOR	0.74	G8V
ASAS J002409-6211.1	HIP 1910	TUC/HOR	1.4	M0Ve
ASAS J003451-6155.0	HIP 2729	TUC/HOR	1.05	K4Ve
ASAS J004220-7747.7	TYC 9351-1110-1	TUC/HOR	1.06	K3Ve
ASAS J011315-6411.6	TYC 8852-0264-1	TUC/HOR	0.87	K1V
ASAS J015749-2154.1	HIP 9141	TUC/HOR	0.65	G4V
ASAS J020136-1610.0	BD-16-351	COL	1.1	K5
ASAS J020718-5311.9	HIP 9892	TUC/HOR	0.65	G7V
ASAS J024126+0559.3	HIP 12545	β Pic	1.21	K6Ve
ASAS J024233-5739.6	TYC 8497-0995-1	TUC/HOR	1.23	K5Ve
ASAS J030942-0934.8	HIP 14684	ABDOR	0.81	G0
ASAS J031909-3507.0	TYC 7026-0325-1	TUC/HOR	1.3	K7Ve
ASAS J033049-4555.9	TYC 8060-1673-1	TUC/HOR	0.95	K3V
ASAS J033156-4359.2	TYC 7574-0803-1	TUC/HOR	1.3	K6Ve
ASAS J034723-0158.3	HIP 17695	ABDOR	1.51	M3
ASAS J045249-1955.0	TYC 5907-1244-1	TUC/HOR	0.87	XX
ASAS J045305-4844.6	TYC 8080-1206-1	COL	0.87	K2V(e)
ASAS J045935+0147.0	HIP 23200	β Pic	1.39	M0.5Ve
ASAS J050047-5715.4	HIP 23309	β Pic	1.4	M0Ve
ASAS J050230-3959.2	TYC 7587-0925-1	ABDOR	0.88	K4V
ASAS J050651+7221.2	CD -72 248	Octans	0.82	K0IV
ASAS J052845-6526.9	HIP 25647	ABDOR	0.83	K0V
ASAS J052857-3328.3	TYC 7059-1111-1	ABDOR	1.06	K3Ve
ASAS J053705-3932.4	TYC 7600-0516-1	TUC/HOR	0.8	K1V(e)
ASAS J055101-5238.2	TYC 8520-0032-1	COL	0.75	G9IV
ASAS J055329-8156.9	TYC 9390-0322-1	CAR	0.79	K0V+VI
ASAS J055751-3804.1	TYC 7598-1488-1	ABDOR	0.69	G6V(e)
ASAS J060834-3402.9	TYC 7079-0068-1	ABDOR	0.79	G9Ve
ASAS J061828-7202.7	HIP 29964	β Pic	1.13	K4Ve
ASAS J062607-4102.9	TYC 7617-0549-1	COL	0.8	K0V
ASAS J062806-4826.9	TYC 8107-1591-1	COL	0.65	G9V
ASAS J063950-6128.7	HIP 31878	ABDOR	1.26	K7Ve
ASAS J064346-7158.6	HIP 32235	CAR	0.7	G6V
ASAS J065623-4646.9	TYC 8118-0871-1	COL	0.78	K0V(e)
ASAS J070030-7941.8	HIP 33737	CAR	0.91	K2V
ASAS J070153-4227.9	CD -42 2906	Argus	0.84	K1V
ASAS J072124-5720.6	TYC 8559-1016-1	CAR	0.64	K0V+D
ASAS J072822-4908.6	CD -48 2972	Argus	0.8	G8V
ASAS J072851-3014.8	HIP 36349	ABDOR	1.44	M1Ve
ASAS J073547-3212.2	HD61005	Argus	0.75	G8V
ASAS J082406-6334.1	TYC 8929-0927-1	CAR	0.63	G5V
ASAS J082844-5205.7	PMM7422	IC2391	0.69	G6
ASAS J083656-7856.8	RECX1	η Cha	1.19	K4Ve
ASAS J084006-5338.1	PMM1083	IC2391	0.57	G0
ASAS J084200-6218.4	TYC 8930-0601-1	CAR	0.8	K0V
ASAS J084229-7903.9	RECX4	η Cha	1.33	K7
ASAS J084300-5354.1	PMM756	IC2391	0.68	G9
ASAS J084432-7846.6	RECX10	η Cha	1.33	K7
ASAS J084708-7859.6	RECX11	η Cha	1.0	K4
ASAS J085005-7554.6	TYC 9395-2139-1	CAR	0.76	G9V
ASAS J085156-5355.9	TYC 8569-3597-1	CAR	0.69	G9V
ASAS J085746-5408.6	TYC 8582-3040-1	CAR	0.88	K2IV
ASAS J085752-4941.8	TYC 8160-0958-1	CAR	0.73	G9V
ASAS J085929-5446.8	TYC 8586-2431-1	CAR	0.6	G5IV
ASAS J092335-6111.6	HIP 46063	CAR	0.86	K1V(e)
ASAS J092854-4101.3	TYC 7695-0335-1	Argus	0.67	K3V
ASAS J094247-7239.8	TYC 9217-0641-1	Argus	0.65	K1V
ASAS J095558-6721.4	HD309851	Argus	0.6	G1V
ASAS J101315-5230.9	TWA 21	TWA	1.0	K3V3

Table 2. continued.

Target ID	Target Name	Assoc.	$B - V$ (mag)	Sp. Type
ASAS J105351-7002.3	CP -69 1432	Argus	0.62	G2V
ASAS J105749-6914.0	CP -68 1388	ϵ Cha	0.86	K1V(e)
ASAS J110914-3001.7	TWA 2	TWA	1.48	M2Ve
ASAS J112105-3845.3	TWA 12	TWA	1.53	M1V
ASAS J112117-3446.8	TWA 13A	TWA	1.42	M1Ve
ASAS J112205-2446.7	TWA 4	TWA	1.17	K5V
ASAS J115942-7601.4	HIP 58490	ϵ Cha	1.11	K4Ve
ASAS J120139-7859.3	HD104467	ϵ Cha	0.63	G5Ve
ASAS J120204-7853.1	GSC 09420-00948	ϵ Cha	1.0	K7e
ASAS J121138-7110.6	HD105923	ϵ Cha	0.73	G8V
ASAS J121531-3948.7	TWA 25	TWA	1.41	M1Ve
ASAS J122023-7407.7	GSC 9239-1572	ϵ Cha	0.97	K7Ve
ASAS J122034-7539.5	CD -74 673	Argus	1.02	K3Ve
ASAS J122105-7116.9	GSC 9235-1702	ϵ Cha	1.2	K7V
ASAS J123921-7502.7	CD -74 712	ϵ Cha	0.97	K3Ve
ASAS J125826-7028.8	CD -69 1055	ϵ Cha	0.83	K0Ve
ASAS J134913-7549.8	CD -75 652	Argus	0.68	G1V
ASAS J153857-5742.5	HIP 76629	β Pic	0.81	K0V
ASAS J171726-6657.1	HIP 84586	β Pic	0.76	G5IV
ASAS J181411-3247.5	V4046-Sgr	β Pic	0.95	K5
ASAS J181952-2916.5	HIP 89829	β Pic	0.69	G1V
ASAS J184653-6210.6	TYC 9073-0762-1	β Pic	1.46	M1Ve
ASAS J185306-5010.8	HIP 92680	β Pic	0.77	K8Ve
ASAS J200724-5147.5	CD -52 9381	Argus	1.24	K6Ve
ASAS J204510-3120.4	HIP 102409	β Pic	1.49	M1Ve
ASAS J205603-1710.9	TYC 6349-0200-1	β Pic	1.22	K6Ve+M
ASAS J212050-5302.0	HIP 105388	TUC/HOR	0.72	G7V
ASAS J214430-6058.6	HIP 107345	TUC/HOR	1.41	M0Ve
ASAS J232749-8613.3	TYC 9529-0340-1	TUC/HOR	0.6	99
ASAS J233231-1215.9	TYC 5832-0666-1	β Pic	1.43	M0Ve
ASAS J234154-3558.7	HIP 116910	ABDOR	0.71	G8V
SWASP1 J002334.66+201428.6	TYC 1186-706-1	β Pic	1.4	K7Ve
SWASP1 J021055.38-460358.6	TYC 8042-1050-1	ABDOR	0.91	K3IVe
SWASP1 J022729.25+305824.6	HIP 11437	β Pic	1.21	K8
SWASP1 J033120.80-303058.7	HIP 16413	COL	0.64	G7IV
SWASP1 J041422.57-381901.5	HIP 19775	COL	0.58	G3V
SWASP1 J042148.68-431732.5	TYC 7584-1630-1	COL	0.69	G7V
SWASP1 J043450.78-354721.2	TYC 7044-0535-1	COL	0.84	K1Ve
SWASP1 J045153.54-464713.3	TYC 8077-0657-1	COL	0.69	G5V
SWASP1 J050649.47-213503.7	BD-21-1074	β Pic	1.52	M2
SWASP1 J051829.04-300132.0	TYC 7048-1453-1	TUC/HOR	1.27	K4Ve
SWASP1 J052855.09-453458.3	TYC 8086-0954-1	COL	0.86	K1V
SWASP1 J053504.11-341751.9	TYC 7064-0839-1	ABDOR	1.08	K4Ve
SWASP1 J054516.24-383649.1	TYC 7597-0833-1	COL	0.68	G9V
SWASP1 J055021.43-291520.7	TYC 6502-1188-1	COL	0.66	K0V(e)
SWASP1 J064118.50-382036.1	TYC 7627-2190-1	ABDOR	1.19	K2e
SWASP1 J101828.70-315002.8	TWA 6	TWA	1.31	M0Ve
SWASP1 J113241.23-265200.7	TWA 8	TWA	1.46	M3Ve
SWASP1 J114824.21-372849.2	TWA 9	TWA	1.26	K5V
SWASP1 J191144.66-260408.5	TYC 6878-0195-1	β Pic	1.05	K4V(e)
SWASP1 J224457.83-331500.6	HIP 112312	β Pic	1.48	M4IVe
SWASP1 J231152.05-450810.6	HIP 114530	ABDOR	0.8	G8V

Notes. The color indexes and spectral types are those reported in Messina et al. (2010, 2011). (See the reference therein for details).

Table 3. Results

Star Id.	$\langle P_{\text{rot}} \rangle$ (d)	Ω_{min} (rad d ⁻¹)	Ω_{max} (rad d ⁻¹)	$\Delta\Omega_{\text{phot}}$ (rad d ⁻¹)	α_{phot} (rad d ⁻¹)	TS	N_{seg}	Qual.
ASAS J001353-7441.3	3.67	1.653 ± 0.013	1.799 ± 0.016	0.146 ± 0.021	0.081 ± 0.012	as	141	B
ASAS J002409-6211.1	1.75	3.558 ± 0.008	3.627 ± 0.012	0.068 ± 0.014	0.019 ± 0.004	as	64	C
ASAS J003451-6155.0	0.38	16.638 ± 0.006	16.695 ± 0.008	0.057 ± 0.01	0.003 ± 0.001	as	79	C
ASAS J004220-7747.7	2.57	2.422 ± 0.012	2.47 ± 0.01	0.048 ± 0.016	0.019 ± 0.006	as	175	B
ASAS J011315-6411.6	1.26	4.956 ± 0.01	5.001 ± 0.005	0.045 ± 0.011	0.009 ± 0.002	as	133	B
ASAS J015749-2154.1	3.05	2.033 ± 0.016	2.119 ± 0.008	0.086 ± 0.018	0.041 ± 0.009	sw	113	B
ASAS J020136-1610.0	3.21	1.909 ± 0.013	1.985 ± 0.012	0.076 ± 0.018	0.038 ± 0.009	as	72	C
ASAS J020718-5311.9	2.33	2.61 ± 0.012	2.843 ± 0.007	0.233 ± 0.014	0.082 ± 0.005	as	63	C
ASAS J024126+0559.3	4.83	1.283 ± 0.008	1.318 ± 0.01	0.035 ± 0.013	0.027 ± 0.01	as	68	C
ASAS J024233-5739.6	7.4	0.816 ± 0.007	0.887 ± 0.011	0.071 ± 0.013	0.08 ± 0.015	as	255	A
ASAS J030942-0934.8	5.47	1.109 ± 0.009	1.177 ± 0.008	0.068 ± 0.012	0.058 ± 0.01	as	45	C
ASAS J031909-3507.0	8.52	0.707 ± 0.012	0.768 ± 0.011	0.061 ± 0.016	0.079 ± 0.021	as	115	B
ASAS J033049-4555.9	3.8	1.591 ± 0.014	1.713 ± 0.009	0.122 ± 0.017	0.071 ± 0.01	as	66	C
ASAS J033156-4359.2	2.93	2.113 ± 0.009	2.182 ± 0.008	0.07 ± 0.012	0.032 ± 0.005	as	89	C
ASAS J034723-0158.3	3.86	1.614 ± 0.01	1.672 ± 0.009	0.057 ± 0.013	0.034 ± 0.008	as	14	C
ASAS J045249-1955.0	5.21	1.178 ± 0.01	1.238 ± 0.01	0.06 ± 0.014	0.049 ± 0.011	as	129	B
ASAS J045305-4844.6	4.59	1.344 ± 0.007	1.403 ± 0.01	0.059 ± 0.012	0.042 ± 0.009	as	153	B
ASAS J045935+0147.0	4.42	1.4 ± 0.009	1.447 ± 0.005	0.047 ± 0.01	0.033 ± 0.007	as	100	B
ASAS J050047-5715.4	8.74	0.694 ± 0.011	0.743 ± 0.007	0.05 ± 0.013	0.067 ± 0.017	as	173	B
ASAS J050230-3959.2	6.58	0.92 ± 0.007	0.993 ± 0.015	0.073 ± 0.017	0.073 ± 0.017	as	247	A
ASAS J050651-7221.2	0.24	26.637 ± 0.012	26.738 ± 0.012	0.101 ± 0.017	0.004 ± 0.001	as	44	C
ASAS J052845-6526.9	0.51	12.189 ± 0.015	12.242 ± 0.013	0.053 ± 0.02	0.004 ± 0.002	as	273	A
ASAS J052857-3328.3	0.69	9.005 ± 0.008	9.075 ± 0.01	0.07 ± 0.013	0.008 ± 0.001	as	43	C
ASAS J053705-3932.4	2.46	2.44 ± 0.007	2.622 ± 0.009	0.182 ± 0.011	0.069 ± 0.004	sw	390	A
ASAS J055101-5238.2	1.2	5.182 ± 0.013	5.263 ± 0.014	0.081 ± 0.021	0.015 ± 0.004	as	122	B
ASAS J055329-8156.9	1.86	3.313 ± 0.012	3.438 ± 0.02	0.125 ± 0.024	0.036 ± 0.007	as	406	A
ASAS J055751-3804.1	0.79	7.911 ± 0.009	8.054 ± 0.011	0.143 ± 0.014	0.018 ± 0.002	as	126	B
ASAS J060834-3402.9	3.4	1.797 ± 0.01	1.897 ± 0.013	0.1 ± 0.018	0.053 ± 0.01	as	119	B
ASAS J061828-7202.7	2.67	2.333 ± 0.013	2.378 ± 0.007	0.045 ± 0.016	0.019 ± 0.007	as	174	B
ASAS J062607-4102.9	4.18	1.451 ± 0.005	1.558 ± 0.009	0.106 ± 0.015	0.068 ± 0.01	sw	147	B
ASAS J062806-4826.9	1.29	4.823 ± 0.015	4.901 ± 0.015	0.078 ± 0.021	0.016 ± 0.004	as	80	C
ASAS J063950-6128.7	9.12	0.666 ± 0.017	0.711 ± 0.01	0.045 ± 0.021	0.064 ± 0.03	as	32	C
ASAS J064346-7158.6	3.89	1.541 ± 0.007	1.669 ± 0.011	0.128 ± 0.013	0.077 ± 0.008	as	155	B
ASAS J065623-4646.9	4.45	1.348 ± 0.02	1.473 ± 0.012	0.124 ± 0.025	0.084 ± 0.017	as	156	B
ASAS J070030-7941.8	5.11	1.189 ± 0.008	1.269 ± 0.01	0.08 ± 0.013	0.063 ± 0.01	as	413	A
ASAS J070153-4227.9	3.99	1.526 ± 0.015	1.641 ± 0.016	0.114 ± 0.022	0.07 ± 0.014	as	230	A
ASAS J072124-5720.6	4.67	1.285 ± 0.015	1.399 ± 0.01	0.114 ± 0.018	0.082 ± 0.013	as	129	B
ASAS J072822-4908.6	1.03	5.996 ± 0.012	6.157 ± 0.012	0.161 ± 0.017	0.026 ± 0.003	as	101	B
ASAS J072851-3014.8	1.64	3.802 ± 0.015	3.849 ± 0.012	0.047 ± 0.019	0.012 ± 0.005	as	226	A
ASAS J073547-3212.2	5.06	1.199 ± 0.019	1.286 ± 0.017	0.087 ± 0.025	0.068 ± 0.02	as	51	C
ASAS J082406-6334.1	0.79	7.842 ± 0.015	8.03 ± 0.019	0.188 ± 0.025	0.023 ± 0.003	as	204	A
ASAS J082844-5205.7	1.51	4.116 ± 0.01	4.21 ± 0.012	0.094 ± 0.016	0.022 ± 0.004	as	169	B
ASAS J083656-7856.8	4.45	1.384 ± 0.007	1.454 ± 0.008	0.07 ± 0.011	0.048 ± 0.008	as	233	A
ASAS J084006-5338.1	1.34	4.662 ± 0.007	4.746 ± 0.01	0.085 ± 0.012	0.018 ± 0.003	as	89	C
ASAS J084200-6218.4	1.22	5.085 ± 0.011	5.183 ± 0.005	0.097 ± 0.012	0.019 ± 0.002	as	140	B
ASAS J084229-7903.9	7.14	0.838 ± 0.014	0.924 ± 0.015	0.087 ± 0.021	0.094 ± 0.023	as	204	A
ASAS J084300-5354.1	3.15	1.957 ± 0.012	2.028 ± 0.011	0.072 ± 0.017	0.035 ± 0.008	as	131	B
ASAS J084432-7846.6	20.26	0.265 ± 0.013	0.336 ± 0.017	0.07 ± 0.022	0.21 ± 0.067	as	74	C
ASAS J084708-7859.6	4.84	1.245 ± 0.014	1.355 ± 0.01	0.111 ± 0.017	0.082 ± 0.013	as	104	B
ASAS J085005-7554.6	1.15	5.433 ± 0.017	5.55 ± 0.016	0.117 ± 0.023	0.021 ± 0.004	as	183	B
ASAS J085156-5355.9	1.91	3.172 ± 0.018	3.397 ± 0.014	0.226 ± 0.023	0.066 ± 0.007	as	81	C
ASAS J085746-5408.6	1.94	3.202 ± 0.022	3.286 ± 0.012	0.084 ± 0.025	0.025 ± 0.007	as	70	C
ASAS J085752-4941.8	2.03	3.005 ± 0.002	3.149 ± 0.009	0.143 ± 0.009	0.045 ± 0.003	as	47	C
ASAS J085929-5446.8	0.44	14.264 ± 0.011	14.375 ± 0.006	0.111 ± 0.013	0.008 ± 0.001	as	162	B
ASAS J092335-6111.6	3.89	1.582 ± 0.018	1.648 ± 0.01	0.066 ± 0.021	0.04 ± 0.013	as	244	A
ASAS J092854-4101.3	0.39	16.011 ± 0.006	16.076 ± 0.008	0.065 ± 0.01	0.004 ± 0.001	as	69	C
ASAS J094247-7239.8	2.31	2.682 ± 0.02	2.751 ± 0.01	0.07 ± 0.022	0.025 ± 0.008	as	143	B
ASAS J095558-6721.4	1.83	3.414 ± 0.016	3.499 ± 0.008	0.085 ± 0.019	0.024 ± 0.005	as	133	B
ASAS J101315-5230.9	4.4	1.388 ± 0.008	1.482 ± 0.014	0.094 ± 0.016	0.063 ± 0.011	as	164	B
ASAS J105351-7002.3	1.03	6.056 ± 0.014	6.157 ± 0.007	0.102 ± 0.017	0.017 ± 0.003	as	32	C

Table 3. continued.

Star Id.	$\langle P_{\text{rot}} \rangle$ (d)	Ω_{min} (rad d ⁻¹)	Ω_{max} (rad d ⁻¹)	$\Delta\Omega_{\text{phot}}$ (rad d ⁻¹)	α_{phot} (rad d ⁻¹)	TS	N_{seg}	Qual.
ASAS J105749-6914.0	3.58	1.728 ± 0.013	1.781 ± 0.006	0.053 ± 0.014	0.03 ± 0.008	as	184	B
ASAS J110914-3001.7	4.85	1.255 ± 0.018	1.341 ± 0.014	0.086 ± 0.023	0.064 ± 0.017	as	102	B
ASAS J112105-3845.3	3.3	1.882 ± 0.011	1.921 ± 0.009	0.039 ± 0.014	0.02 ± 0.007	as	138	B
ASAS J112117-3446.8	5.44	1.108 ± 0.007	1.187 ± 0.003	0.079 ± 0.008	0.067 ± 0.007	sw	352	A
ASAS J112205-2446.7	14.3	0.413 ± 0.015	0.469 ± 0.014	0.056 ± 0.021	0.119 ± 0.045	as	108	B
ASAS J115942-7601.4	8.04	0.756 ± 0.011	0.808 ± 0.011	0.052 ± 0.016	0.065 ± 0.02	as	87	C
ASAS J120139-7859.3	4.38	1.368 ± 0.012	1.492 ± 0.018	0.124 ± 0.022	0.083 ± 0.015	as	34	C
ASAS J120204-7853.1	4.44	1.393 ± 0.005	1.434 ± 0.023	0.041 ± 0.024	0.028 ± 0.016	as	161	B
ASAS J121138-7110.6	5.13	1.182 ± 0.008	1.28 ± 0.009	0.098 ± 0.012	0.076 ± 0.009	as	107	B
ASAS J121531-3948.7	5.06	1.216 ± 0.017	1.263 ± 0.008	0.047 ± 0.019	0.037 ± 0.015	as	224	A
ASAS J122023-7407.7	1.54	4.052 ± 0.013	4.129 ± 0.017	0.077 ± 0.022	0.019 ± 0.005	as	167	B
ASAS J122034-7539.5	3.49	1.756 ± 0.007	1.844 ± 0.015	0.088 ± 0.017	0.048 ± 0.009	as	178	B
ASAS J122105-7116.9	6.86	0.892 ± 0.005	0.942 ± 0.011	0.05 ± 0.012	0.053 ± 0.013	as	113	B
ASAS J123921-7502.7	3.99	1.548 ± 0.008	1.598 ± 0.01	0.05 ± 0.013	0.031 ± 0.008	as	331	A
ASAS J125826-7028.8	2.0	3.13 ± 0.013	3.178 ± 0.011	0.048 ± 0.017	0.015 ± 0.005	as	49	C
ASAS J134913-7549.8	2.29	2.703 ± 0.014	2.802 ± 0.009	0.1 ± 0.017	0.036 ± 0.006	as	171	B
ASAS J153857-5742.5	4.3	1.412 ± 0.014	1.517 ± 0.011	0.105 ± 0.018	0.069 ± 0.012	as	210	A
ASAS J171726-6657.1	1.68	3.691 ± 0.016	3.809 ± 0.015	0.119 ± 0.023	0.031 ± 0.006	as	168	B
ASAS J181411-3247.5	2.42	2.553 ± 0.003	2.65 ± 0.007	0.097 ± 0.008	0.037 ± 0.003	as	98	C
ASAS J181952-2916.5	0.57	10.969 ± 0.013	11.066 ± 0.013	0.097 ± 0.018	0.009 ± 0.002	as	194	B
ASAS J184653-6210.6	5.37	1.146 ± 0.009	1.199 ± 0.012	0.053 ± 0.015	0.044 ± 0.012	as	88	C
ASAS J185306-5010.8	0.94	6.625 ± 0.012	6.696 ± 0.014	0.072 ± 0.018	0.011 ± 0.003	as	39	C
ASAS J200724-5147.5	0.84	7.484 ± 0.011	7.521 ± 0.005	0.036 ± 0.012	0.005 ± 0.002	as	62	C
ASAS J204510-3120.4	4.84	1.269 ± 0.009	1.334 ± 0.012	0.065 ± 0.015	0.049 ± 0.011	as	31	C
ASAS J205603-1710.9	3.4	1.828 ± 0.008	1.87 ± 0.015	0.042 ± 0.017	0.023 ± 0.009	as	35	C
ASAS J212050-5302.0	3.43	1.711 ± 0.018	1.906 ± 0.01	0.195 ± 0.021	0.102 ± 0.011	as	108	B
ASAS J214430-6058.6	4.55	1.342 ± 0.006	1.428 ± 0.017	0.086 ± 0.018	0.06 ± 0.013	as	52	C
ASAS J232749-8613.3	0.7	8.882 ± 0.011	9.05 ± 0.017	0.168 ± 0.02	0.019 ± 0.002	as	226	A
ASAS J233231-1215.9	5.69	1.086 ± 0.007	1.117 ± 0.009	0.031 ± 0.011	0.028 ± 0.01	as	42	C
ASAS J234154-3558.7	1.79	3.419 ± 0.017	3.566 ± 0.005	0.147 ± 0.018	0.041 ± 0.005	sw	242	A
SWASP1 J002334.66+201428.6	7.88	0.753 ± 0.02	0.841 ± 0.009	0.088 ± 0.025	0.105 ± 0.03	sw	401	A
SWASP1 J021055.38-460358.6	1.12	5.586 ± 0.008	5.664 ± 0.005	0.077 ± 0.01	0.014 ± 0.002	sw	131	B
SWASP1 J022729.25+305824.6	12.43	0.365 ± 0.01	0.521 ± 0.013	0.156 ± 0.018	0.299 ± 0.035	sw	142	B
SWASP1 J033120.80-303058.7	1.85	3.355 ± 0.006	3.418 ± 0.006	0.063 ± 0.008	0.018 ± 0.002	sw	192	B
SWASP1 J041422.57-381901.5	1.69	3.672 ± 0.013	3.769 ± 0.012	0.097 ± 0.018	0.026 ± 0.005	sw	147	B
SWASP1 J042148.68-431732.5	1.95	3.158 ± 0.015	3.284 ± 0.005	0.126 ± 0.016	0.038 ± 0.005	sw	243	A
SWASP1 J043450.78-354721.2	2.3	2.65 ± 0.017	2.773 ± 0.003	0.123 ± 0.023	0.044 ± 0.008	sw	298	A
SWASP1 J045153.54-464713.3	2.84	2.161 ± 0.007	2.239 ± 0.012	0.078 ± 0.014	0.035 ± 0.006	sw	223	A
SWASP1 J050649.47-213503.7	13.39	0.453 ± 0.007	0.508 ± 0.01	0.055 ± 0.012	0.108 ± 0.024	sw	227	A
SWASP1 J051829.04-300132.0	1.7	3.686 ± 0.008	3.725 ± 0.007	0.039 ± 0.011	0.01 ± 0.003	sw	223	A
SWASP1 J052855.09-453458.3	4.68	1.298 ± 0.009	1.397 ± 0.004	0.099 ± 0.01	0.071 ± 0.007	sw	277	A
SWASP1 J053504.11-341751.9	1.15	5.472 ± 0.003	5.495 ± 0.004	0.023 ± 0.005	0.004 ± 0.001	sw	310	A
SWASP1 J054516.24-383649.1	1.35	4.573 ± 0.007	4.685 ± 0.003	0.112 ± 0.008	0.024 ± 0.002	sw	218	A
SWASP1 J055021.43-291520.7	3.47	1.76 ± 0.005	1.872 ± 0.006	0.112 ± 0.008	0.06 ± 0.004	sw	276	A
SWASP1 J064118.50-382036.1	0.73	8.576 ± 0.009	8.686 ± 0.008	0.109 ± 0.012	0.013 ± 0.001	sw	310	A
SWASP1 J101828.70-315002.8	0.54	11.591 ± 0.007	11.629 ± 0.006	0.038 ± 0.009	0.003 ± 0.001	sw	474	A
SWASP1 J113241.23-265200.7	4.64	1.346 ± 0.002	1.376 ± 0.004	0.03 ± 0.004	0.022 ± 0.003	sw	325	A
SWASP1 J114824.21-372849.2	5.04	1.215 ± 0.011	1.273 ± 0.013	0.058 ± 0.018	0.046 ± 0.014	sw	252	A
SWASP1 J191144.66-260408.5	5.73	1.071 ± 0.005	1.132 ± 0.006	0.061 ± 0.008	0.054 ± 0.007	sw	192	B
SWASP1 J224457.83-331500.6	2.36	2.627 ± 0.014	2.7 ± 0.007	0.074 ± 0.02	0.027 ± 0.007	sw	265	A
SWASP1 J231152.05-450810.6	5.16	1.176 ± 0.013	1.266 ± 0.009	0.09 ± 0.017	0.071 ± 0.013	sw	87	C

Notes. For each source, we reported the average rotation period, the minimum and maximum detected angular frequencies, the corresponding $\Delta\Omega_{\text{phot}}$ and the relative shear α_{phot} . Next to each quantity we also reported the estimated error. In the last three columns we reported a time-series flag indicating whether the results have been inferred with ASAS or Super WASP time-series, the number N of segments in which a significant period has been detected and a quality flag related to N . The flag A is assigned to stars with $N > 200$, the flag B to stars with N between 100 and 200 and the flag C to stars with $N < 100$.

Table 4. Data used to compute absolute magnitudes

Target ID	parallax (mas)	distance (pc)	DM (mag)	M_J (mag)	M_H (mag)	Ref.
ASAS J001353-7441.3	22.8	43.86	3.21	4.20	3.88	1
ASAS J002409-6211.1	21.6	46.30	3.33	5.06	4.38	1
ASAS J003451-6155.0	21.8	45.87	3.31	4.03	3.41	1
ASAS J004220-7747.7		50.00	3.49	4.73	4.16	2
ASAS J011315-6411.6	17.1	58.48	3.83	4.78	4.29	3
ASAS J015749-2154.1	23.6	42.37	3.14	3.72	3.42	1
ASAS J020136-1610.0		92.00	4.82	3.79	3.28	2
ASAS J020718-5311.9	19.9	50.25	3.51	3.84	3.48	1
ASAS J024126+0559.3	24.7	40.49	3.04	4.87	4.20	1
ASAS J024233-5739.6		50.00	3.49	5.07	4.47	2
ASAS J030942-0934.8	26.73	37.41	2.87	4.29	3.93	3
ASAS J031909-3507.0		44.00	3.22	5.36	4.70	2
ASAS J033049-4555.9		44.00	3.22	4.55	4.03	2
ASAS J033156-4359.2		42.00	3.12	5.18	4.56	2
ASAS J034723-0158.3	62.0	16.13	1.04	6.77	6.14	3
ASAS J045249-1955.0		72.00	4.29	3.76	3.21	2
ASAS J045305-4844.6		76.00	4.40	4.46	4.02	2
ASAS J045935+0147.0	37.5	26.67	2.13	4.99	4.32	1
ASAS J050047-5715.4	38.1	26.25	2.10	5.00	4.33	1
ASAS J050230-3959.2		42.00	3.12	5.61	5.09	2
ASAS J050651+7221.2		143.00	5.78			2
ASAS J052845-6526.9	66.9	14.95	.87	4.44	3.97	1
ASAS J052857-3328.3		57.00	3.78	4.65	4.14	2
ASAS J053705-3932.4	18.87	52.99	3.62	4.28	3.84	3
ASAS J055101-5238.2		106.00	5.13	3.96	3.56	2
ASAS J055329-8156.9		59.00	3.85	3.68	3.19	2
ASAS J055751-3804.1		68.00	4.16	3.97	3.58	2
ASAS J060834-3402.9		72.00	4.29	4.43	4.04	2
ASAS J061828-7202.7	25.9	38.61	2.93	4.60	4.05	1
ASAS J062607-4102.9		91.00	4.80	3.74	3.36	2
ASAS J062806-4826.9		135.00	5.65	3.88	3.46	2
ASAS J063950-6128.7	45.6	21.93	1.71	5.60	4.94	1
ASAS J064346-7158.6	17.7	56.50	3.76	3.93	3.62	1
ASAS J065623-4646.9		75.00	4.38	4.01	3.52	2
ASAS J070030-7941.8	15.6	64.10	4.03	4.23	3.80	1
ASAS J070153-4227.9	10.7	93.46	4.85			5
ASAS J072124-5720.6		100.00	5.00	4.21	3.78	2
ASAS J072822-4908.6	12.6	79.37	4.50	4.01	3.63	5
ASAS J072851-3014.8	64.2	15.58	.96	5.65	5.01	1
ASAS J073547-3212.2	28.29	35.35	2.74	4.16	3.84	3
ASAS J082406-6334.1		104.00	5.09	3.48	3.15	2
ASAS J082844-5205.7		120.00	5.40	3.92	3.66	2
ASAS J083656-7856.8		99.00	4.98	3.18	2.52	2
ASAS J084006-5338.1		139.00	5.72	3.61	3.32	2
ASAS J084200-6218.4		147.00	5.84	3.56	3.13	2
ASAS J084229-7903.9		97.30	4.94	4.59	3.84	4
ASAS J084300-5354.1		149.00	5.87	3.89	3.51	2
ASAS J084432-7846.6		97.30	4.94	4.71	3.98	4
ASAS J084708-7859.6		97.30	4.94	3.79	3.09	4
ASAS J085005-7554.6		101.00	5.02	4.24	3.83	2
ASAS J085156-5355.9		141.00	5.75	3.57	3.15	2
ASAS J085746-5408.6		159.00	6.01	3.90	3.47	2
ASAS J085752-4941.8		111.00	5.23	3.86	3.53	2
ASAS J085929-5446.8		106.00	5.13	3.66	3.33	2
ASAS J092335-6111.6	11.8	84.75	4.64	3.92	3.42	1
ASAS J092854-4101.3	6.7	149.25	5.87	3.92	3.40	5
ASAS J094247-7239.8	6.5	153.85	5.94	4.51	4.07	5
ASAS J095558-6721.4	9.2	108.70	5.18	3.52	3.20	5
ASAS J101315-5230.9		48.00	3.41	4.46	3.95	2

Table 4. continued.

Target ID	distance (pc)	parallax (mas)	DM (mag)	M_J (mag)	M_H (mag)	Ref.
ASAS J105351-7002.3	6.3	158.73	6.00	3.43	3.15	5
ASAS J105749-6914.0		112.00	5.25	3.24	2.76	6
ASAS J110914-3001.7		41.00	3.06	4.57	3.86	2
ASAS J112105-3845.3	31.25	32.00	2.53	6.47	5.81	3
ASAS J112117-3446.8		55.00	3.70	4.73	4.03	2
ASAS J112205-2446.7	21.4	46.73	3.35	3.05	2.41	1
ASAS J115942-7601.4	10.8	107.00	5.15	3.99	3.32	6
ASAS J120139-7859.3		102.00	5.04	2.22	1.92	6
ASAS J120204-7853.1		110.00	5.21	4.01	3.25	6
ASAS J121138-7110.6		112.00	5.25	2.43	2.06	6
ASAS J121531-3948.7		51.00	3.54	4.63	3.97	2
ASAS J122023-7407.7		110.00	5.21	4.05	3.40	6
ASAS J122034-7539.5	19.5	51.28	3.55	5.03	4.54	5
ASAS J122105-7116.9		100.00	5.00	4.09	3.42	6
ASAS J123921-7502.7		100.00	5.00	3.43	2.95	6
ASAS J125826-7028.8		99.00	4.98	3.21	2.72	6
ASAS J134913-7549.8	12.3	81.30	4.55	3.82	3.48	5
ASAS J153857-5742.5	25.2	39.68	2.99	3.39	3.00	1
ASAS J171726-6657.1	31.8	31.45	2.49	2.80	2.42	1
ASAS J181411-3247.5		73.00	4.32	3.75	3.12	2
ASAS J181952-2916.5	13.3	75.19	4.38	3.15	2.82	1
ASAS J184653-6210.6		54.00	3.66	5.08	4.39	2
ASAS J185306-5010.8	20.1	49.75	3.48	3.37	3.00	1
ASAS J200724-5147.5	33.6	29.76	2.37	5.79	5.20	5
ASAS J204510-3120.4	100.6	9.94	-.01	5.45	4.84	1
ASAS J205603-1710.9		47.00	3.36	4.49	3.89	2
ASAS J212050-5302.0	21.8	45.87	3.31	4.08	3.72	1
ASAS J214430-6058.6	23.6	42.37	3.14	5.62	4.95	1
ASAS J232749-8613.3		60.00	3.89	4.06	3.70	2
ASAS J233231-1215.9		28.00	2.24	5.21	4.53	2
ASAS J234154-3558.7	16.0	62.50	3.98	4.12	3.79	1
SWASP1 J002334.66+201428.6		31.00	2.46	5.68	5.04	2
SWASP1 J021055.38-460358.6		70.00	4.23	5.06	4.53	2
SWASP1 J022729.25+305824.6	25.03	39.95	3.01	4.86	4.23	3
SWASP1 J033120.80-303058.7	7.8	128.21	5.54	2.93	2.58	1
SWASP1 J041422.57-381901.5	12.1	82.64	4.59	3.36	3.11	3
SWASP1 J042148.68-431732.5		143.00	5.78	3.14	2.76	2
SWASP1 J043450.78-354721.2		77.00	4.43	4.86	4.32	2
SWASP1 J045153.54-464713.3		80.00	4.52	4.03	3.68	2
SWASP1 J050649.47-213503.7		18.00	1.28	5.77	5.11	2
SWASP1 J051829.04-300132.0		65.00	4.06	5.07	4.38	2
SWASP1 J052855.09-453458.3		78.00	4.46	5.10	4.61	2
SWASP1 J053504.11-341751.9		78.00	4.46	5.34	4.79	2
SWASP1 J054516.24-383649.1		90.00	4.77	4.79	4.38	2
SWASP1 J055021.43-291520.7		149.00	5.87	3.77	3.38	2
SWASP1 J064118.50-382036.1		78.00	4.46	5.02	4.48	2
SWASP1 J101828.70-315002.8	12.99	76.98	4.43	4.44	3.75	3
SWASP1 J113241.23-265200.7		39.00	2.96			2
SWASP1 J114824.21-372849.2	19.9	50.25	3.51	5.18	4.53	1
SWASP1 J191144.66-260408.5		80.00	4.52	3.57	3.04	2
SWASP1 J224457.83-331500.6	42.4	23.58	1.86	5.92	5.29	1
SWASP1 J231152.05-450810.6	19.7	50.76	3.53	3.94	3.58	1

Notes. For each target we reported the distance or the parallax reported in previous works, the distance modulus and the absolute J H magnitudes inferred in the present work. In the last column we reported the reference from which the distance or the parallax has been taken. References: (1) Torres et al. (2006); (2) Torres et al. (2008); (3) Perryman et al. (1997); (4) Mamajek et al. (2000); (5) De Silva et al. (2013); (6) Murphy et al. (2013).

Table 5. Stellar parameters inferred by the comparison of J and H magnitudes with different theoretical models.

Target ID	M_{Siess} (M_{\odot})	T_{Siess} (K)	M_{Baraffe} (M_{\odot})	T_{Baraffe} (K)	M_{Spada} (M_{\odot})	T_{Spada} (K)	τ_{C} (d)	Rosby nr.
ASAS J001353-7441.3	0.92	4764.88	0.93	4464.05	0.95	5060.67	49.717	0.074
ASAS J002409-6211.1	0.79	4199.02	0.8	3997.71	0.78	4325.44	146.045	0.012
ASAS J003451-6155.0	0.99	5164.99	0.98	4727.36	1.03	5446.5	31.85	0.012
ASAS J004220-7747.7	0.84	4407.14	0.86	4165.18	0.86	4608.72	92.809	0.028
ASAS J011315-6411.6	0.83	4334.69	0.84	4109.04	0.83	4513.54	118.681	0.011
ASAS J015749-2154.1	1.03	5348.77	1.0	4861.71	1.06	5596.57	24.489	0.124
ASAS J020136-1610.0	1.05	5416.15	1.01	4897.35	1.07	5649.15	24.489	0.131
ASAS J020718-5311.9	1.0	5224.06	0.99	4774.86	1.04	5499.37	31.85	0.073
ASAS J024126+0559.3	0.78	4049.27	0.78	3827.04	0.83	4115.02	195.566	0.025
ASAS J024233-5739.6	0.77	4164.55	0.79	3971.28	0.77	4263.07	146.045	0.051
ASAS J030942-0934.8	0.96	5185.52	0.91	4982.03	0.95	5545.63	38.991	0.14
ASAS J031909-3507.0	0.69	3999.56	0.73	3852.94	0.71	4000.66	171.965	0.05
ASAS J033049-4555.9	0.87	4524.9	0.88	4272.77	0.89	4764.23	92.809	0.041
ASAS J033156-4359.2	0.74	4097.0	0.77	3919.74	0.74	4151.49	171.965	0.017
ASAS J034723-0158.3	0.45	3751.22	0.48	3627.29	0.49	3684.28	173.081	0.022
ASAS J045249-1955.0	1.07	5496.24	1.02	4956.87	1.08	5709.79	24.489	0.213
ASAS J045305-4844.6	0.88	4564.63	0.89	4311.88	0.9	4820.09	70.606	0.065
ASAS J045935+0147.0	0.73	3992.85	0.74	3783.13	0.8	4015.72	195.566	0.023
ASAS J050047-5715.4	0.73	3986.81	0.74	3778.59	0.8	4005.8	195.566	0.045
ASAS J050230-3959.2	0.67	4184.49	0.64	4111.98	0.68	4320.15	75.111	0.088
ASAS J050651-7221.2	1.2	5872.15	1.06	5236.3	1.13	5996.48	21.57	0.011
ASAS J052845-6526.9	0.93	5103.88	0.88	4894.7	0.93	5455.8	44.701	0.011
ASAS J052857-3328.3	0.88	4936.3	0.84	4752.25	0.88	5274.9	49.528	0.014
ASAS J053705-3932.4	0.92	4741.35	0.92	4444.53	0.95	5038.04	49.717	0.05
ASAS J055101-5238.2	0.98	5101.79	0.97	4689.95	1.02	5392.94	31.85	0.038
ASAS J055329-8156.9	1.08	5564.02	1.02	5007.28	1.09	5760.17	24.489	0.076
ASAS J055751-3804.1	1.04	5462.61	1.01	5292.01	1.04	5862.33	32.162	0.024
ASAS J060834-3402.9	0.93	5079.95	0.88	4872.36	0.92	5427.25	44.701	0.076
ASAS J061828-7202.7	0.87	4177.56	0.86	3918.0	0.88	4302.06	173.338	0.015
ASAS J062607-4102.9	1.04	5384.07	1.0	4878.44	1.07	5623.8	24.489	0.171
ASAS J062806-4826.9	1.0	5209.3	0.99	4766.8	1.04	5490.63	31.85	0.041
ASAS J063950-6128.7	0.69	4231.9	0.66	4162.5	0.69	4383.69	75.111	0.121
ASAS J064346-7158.6	0.97	5076.36	0.97	4674.16	1.02	5370.69	31.85	0.122
ASAS J065623-4646.9	0.98	5100.6	0.97	4686.36	1.02	5390.86	31.85	0.14
ASAS J070030-7941.8	0.93	4799.47	0.93	4482.09	0.96	5097.57	49.717	0.103
ASAS J072124-5720.6	0.93	4817.17	0.93	4493.68	0.97	5115.58	49.717	0.094
ASAS J072822-4908.6	1.02	5388.54	0.92	4920.61	1.02	5578.2	31.956	0.032
ASAS J072851-3014.8	0.67	4196.56	0.65	4122.64	0.68	4336.36	75.111	0.022
ASAS J073547-3212.2	0.94	5158.73	0.89	4724.24	0.97	5390.66	35.458	0.143
ASAS J082406-6334.1	1.15	5751.56	1.04	5131.28	1.11	5886.94	21.575	0.037
ASAS J082844-5205.7	1.03	5415.05	0.93	4972.31	1.03	5615.66	32.309	0.047
ASAS J083656-7856.8	1.41	4863.64	1.36	4459.57				
ASAS J084006-5338.1	1.12	5688.16	1.09	5497.24	1.1	5945.58	21.027	0.064
ASAS J084200-6218.4	1.14	5723.08	1.04	5103.57	1.11	5858.1	21.575	0.057
ASAS J084229-7903.9	0.72	3967.34	0.67	3683.61	0.82	3974.45	306.563	0.023
ASAS J084300-5354.1	1.05	5494.3	0.95	5104.5	1.05	5709.71	27.17	0.116
ASAS J084432-7846.6	0.66	3913.33	0.62	3645.25	0.75	3870.19	338.808	0.06
ASAS J084708-7859.6	1.14	4410.09	1.07	4063.22	1.12	4690.61	175.865	0.028
ASAS J085005-7554.6	0.92	4776.04	0.93	4467.9	0.96	5073.41	49.717	0.023
ASAS J085156-5355.9	1.13	5694.86	1.04	5089.11	1.11	5843.03	21.575	0.089
ASAS J085746-5408.6	0.99	5192.59	0.98	4754.38	1.04	5475.28	31.85	0.061
ASAS J085752-4941.8	0.99	5173.56	0.98	4741.8	1.03	5456.74	31.85	0.064
ASAS J085929-5446.8	1.06	5463.98	1.01	4933.05	1.08	5683.11	24.489	0.018
ASAS J092335-6111.6	1.0	5216.98	0.99	4769.42	1.04	5496.23	31.85	0.122
ASAS J092854-4101.3	1.07	5533.54	1.0	5242.54	1.06	5751.23	27.07	0.014
ASAS J094247-7239.8	0.86	4804.63	0.85	4479.31	0.9	5090.13	41.081	0.056
ASAS J095558-6721.4	1.17	5796.62	1.12	5577.32	1.13	6066.08	21.867	0.083
ASAS J101315-5230.9	0.79	4039.73	0.78	3778.3	0.9	4147.98	219.272	0.02
ASAS J105351-7002.3	1.19	5856.48	1.14	5622.04	1.14	6140.48	21.867	0.047

Table 5. continued.

Target ID	M_{Siess} (M_{\odot})	T_{Siess} (K)	M_{Baraffe} (M_{\odot})	T_{Baraffe} (K)	M_{Spada} (M_{\odot})	T_{Spada} (K)	τ_{C} (d)	Rossby nr.
ASAS J105749-6914.0	1.16	4373.67	1.12	4012.34	1.2	4685.66	233.527	0.015
ASAS J110914-3001.7	0.79	4031.79	0.77	3774.52	0.9	4146.39	219.272	0.022
ASAS J112105-3845.3	0.18	3248.14	0.23	3283.66	0.24	3321.61	464.318	0.007
ASAS J112117-3446.8	0.71	3962.67	0.7	3719.79	0.84	4013.62	269.414	0.02
ASAS J112205-2446.7	1.41	5111.29						
ASAS J115942-7601.4	0.75	4021.5	0.79	3729.38	0.86	4131.34	398.782	0.02
ASAS J120139-7859.3	1.81	4936.73						
ASAS J120204-7853.1	0.76	4036.83	0.79	3730.57	0.88	4162.21	398.782	0.011
ASAS J121138-7110.6	1.7	4828.8						
ASAS J121531-3948.7	0.75	3996.59	0.74	3747.22	0.87	4076.6	244.451	0.021
ASAS J122023-7407.7	0.71	3985.11	0.76	3709.42	0.83	4073.53	442.914	0.003
ASAS J122034-7539.5	0.76	4304.98	0.78	4110.09	0.75	4436.18	103.142	0.034
ASAS J122105-7116.9	0.69	3971.33	0.74	3700.36	0.82	4052.4	442.914	0.015
ASAS J123921-7502.7	1.03	4276.23	0.98	3868.27	1.09	4514.39	283.183	0.014
ASAS J125826-7028.8	1.19	4392.09	1.15	4041.77	1.23	4715.63	233.527	0.009
ASAS J134913-7549.8	1.07	5532.3	0.98	5212.66	1.06	5745.5	27.07	0.084
ASAS J153857-5742.5	1.18	5137.52	1.16	4707.41	1.14	5642.4	68.336	0.063
ASAS J171726-6657.1	1.28	5678.07	1.27	5278.14				
ASAS J181411-3247.5	1.13	4912.49	1.11	4520.86	1.09	5366.58	86.862	0.028
ASAS J181952-2916.5	1.22	5334.97	1.2	4899.31				
ASAS J184653-6210.6	0.7	3955.99	0.71	3755.56	0.78	3955.37	222.362	0.024
ASAS J185306-5010.8	1.18	5144.63	1.16	4714.0	1.14	5651.12	68.336	0.014
ASAS J200724-5147.5	0.59	3897.56	0.6	3684.73	0.62	3826.1	184.707	0.005
ASAS J204510-3120.4	0.54	3806.89	0.58	3625.95	0.62	3721.1	314.173	0.015
ASAS J205603-1710.9	0.92	4271.71	0.9	3991.7	0.91	4447.94	147.384	0.023
ASAS J212050-5302.0	0.95	4933.09	0.95	4573.6	0.99	5233.2	49.717	0.069
ASAS J214430-6058.6	0.62	3896.88	0.67	3758.79	0.65	3823.77	200.199	0.023
ASAS J232749-8613.3	0.95	4953.28	0.95	4587.34	0.99	5252.98	49.717	0.014
ASAS J233231-1215.9	0.65	3904.13	0.67	3709.93	0.73	3859.11	254.116	0.022
ASAS J234154-3558.7	1.0	5317.63	0.96	5156.84	0.99	5696.24	38.991	0.046
SWASP1 J002334.66+201428.6	0.47	3732.26	0.51	3563.56	0.55	3642.87	350.494	0.022
SWASP1 J021055.38-460358.6	0.79	4561.22	0.76	4476.24	0.78	4857.86	62.811	0.018
SWASP1 J022729.25+305824.6	0.78	4043.37	0.78	3822.18	0.83	4103.71	195.566	0.064
SWASP1 J033120.80-303058.7	1.37	6297.53	1.31	6078.61				
SWASP1 J041422.57-381901.5	1.2	5870.07	1.06	5223.15	1.13	5981.71	21.575	0.078
SWASP1 J042148.68-431732.5	1.29	6071.67	1.24	5882.23				
SWASP1 J043450.78-354721.2	0.82	4289.73	0.83	4071.42	0.82	4456.16	118.681	0.019
SWASP1 J045153.54-464713.3	0.96	4985.07	0.96	4609.35	1.0	5283.93	31.85	0.089
SWASP1 J050649.47-213503.7	0.45	3704.11	0.49	3541.96	0.52	3616.87	405.198	0.033
SWASP1 J051829.04-300132.0	0.79	4195.07	0.8	3994.46	0.78	4318.64	146.045	0.012
SWASP1 J052855.09-453458.3	0.74	4105.35	0.77	3930.63	0.75	4167.13	146.045	0.032
SWASP1 J053504.11-341751.9	0.73	4368.41	0.71	4293.5	0.72	4568.21	70.363	0.016
SWASP1 J054516.24-383649.1	0.82	4293.94	0.83	4081.86	0.82	4455.43	118.681	0.011
SWASP1 J055021.43-291520.7	1.03	5349.2	1.0	4855.19	1.06	5597.84	24.489	0.142
SWASP1 J064118.50-382036.1	0.79	4592.53	0.77	4506.23	0.79	4908.82	62.811	0.012
SWASP1 J101828.70-315002.8	0.85	4101.65	0.83	3819.12	0.94	4253.52	219.272	0.002
SWASP1 J114824.21-372849.2	0.51	3775.15	0.52	3575.22	0.62	3714.79	423.631	0.012
SWASP1 J191144.66-260408.5	1.16	5037.76	1.14	4621.4	1.12	5518.4	68.336	0.084
SWASP1 J224457.83-331500.6	0.39	3645.74	0.44	3499.12	0.47	3567.25	487.059	0.005
SWASP1 J231152.05-450810.6	1.04	5472.7	1.01	5301.17	1.04	5873.77	32.162	0.16